

AstroSat-CZTI detection of variable prompt emission polarization in GRB 171010A

VIKAS CHAND^{†,1}, TANMOY CHATTOPADHYAY^{‡,2}, GOR OGANESYAN^{*,3,4}, A. R. RAO¹, SANTOSH V. VADAWALE⁵,
DIPANKAR BHATTACHARYA⁶, V. B. BHALERAO⁷ AND KUNTAL MISRA^{8,9}

¹Tata Institute of Fundamental Research, Mumbai, India

²Pennsylvania State University, State College, PA, USA

³Gran Sasso Science Institute, Viale F. Crispi 7, I-67100, LAquila, Italy

⁴INFN - Laboratori Nazionali del Gran Sasso, I-67100 LAquila, Italy

⁵Physical Research Laboratory, Ahmedabad, Gujarat, India

⁶The Inter-University Centre for Astronomy and Astrophysics, Pune, India

⁷Indian Institute of Technology, Bombay, India

⁸Aryabhata Research Institute of observational scieeES (ARIES), Manora Peak, Nainital, India

⁹Department of Physics, University of California, 1 Shields Ave, Davis, CA 95616-5270, USA

ABSTRACT

We present spectro-polarimetric analysis of GRB 171010A using data from *AstroSat*, *Fermi*, and *Swift*, to provide insights into the physical mechanisms of the prompt radiation and the jet geometry.

Prompt emission from GRB 171010A was very bright (fluence $> 10^{-4}$ ergs cm⁻²) and had a complex structure composed of the superimposition of several pulses. The energy spectra deviate from the typical Band function to show a low energy peak ~ 15 keV — which we interpret as a power-law with two breaks, with a synchrotron origin. Alternately, the prompt spectra can also be interpreted as Comptonized emission, or a blackbody combined with a Band function. Time-resolved analysis confirms the presence of the low energy component, while the peak energy is found to be confined in the range of 100–200 keV.

Afterglow emission detected by *Fermi*-LAT is typical of an external shock model, and we constrain the initial Lorentz factor using the peak time of the emission. *Swift*-XRT measurements of the afterglow show an indication for a jet break, allowing us to constrain the jet opening angle to $> 6^\circ$.

Detection of a large number of Compton scattered events by *AstroSat*-CZTI provides an opportunity to study hard X-ray polarization of the prompt emission. We find that the burst has high, time-variable polarization, with the emission **have higher polarization** at energies above the peak energy.

We discuss all observations in the context of GRB models and polarization arising due to **due to physical or geometric effects**: synchrotron emission from multiple shocks with ordered or random magnetic fields, Poynting flux dominated jet undergoing abrupt magnetic dissipation, sub-photospheric dissipation, a jet consisting of fragmented fireballs, and the Comptonization model.

Keywords: gamma-ray burst: general – gamma-ray burst: individual (GRB 171010A) – polarization – radiation mechanisms: non-thermal

1. INTRODUCTION

The emission mechanisms of gamma ray bursts (GRBs) and the radiation processes involved in producing the complex structure during the prompt phase have eluded a complete understanding in spite of the fact

that these energetic cosmological events have been studied for more than five decades. Based on the duration of the observed prompt emission, GRBs are broadly classified into two families named as long and short GRBs with a demarcation at 2 s. The long GRBs are found to be associated with with type Ic supernovae pointing at their massive star origin. To extract energy efficiently to power a GRB such a collapse results in a black hole or a rapidly spinning and highly magnetized neutron star (Woosley & Bloom 2006; Cano et al. 2017). The recent

[†]vikas.chand.physics@gmail.com

[‡]txc344@psu.edu

*gor.oganesyan@gssi.it

groundbreaking discovery of gravitational waves and its electromagnetic counterpart object (a short GRB) resolved the problem of identifying progenitors of short GRBs at least for the case of one joint GW/GRB detection (Abbott et al. 2016). The commonly accepted scenario for the production of the emerging radiation is based on the premise of relativistic jets being launched from the central engine. When the jet pierces through an ambient medium which is either a constant density interstellar medium (ISM) or a wind-like medium whose density varies with distance, external shocks are formed and the generated radiation has contributions from both the forward and the reverse shocks. The resultant emission constitutes the widely observed afterglows in GRBs (Rees & Meszaros 1992; Meszaros & Rees 1993; Mészáros & Rees 1997; Akerlof et al. 1999; Mészáros & Rees 1999). A plateau phase in the X-ray emission is, however, thought to be associated with a long term central engine activity or the stratification in Lorentz factor of the ejecta could also give extended energy injection (Dai & Lu 1998; Zhang et al. 2006).

The prompt emission can arise due to various mechanisms, the leading candidates among them are: (i) increase of the jet Lorentz factor with time, leading to the collision of inner layers with the outer ones, generating internal shocks which produce non-thermal synchrotron emission as the electrons gyrate in the existing magnetic field (Narayan et al. 1992; Rees & Meszaros 1994). A variant of internal shock model is the Internal-Collision-induced MAGnetic Reconnection and Turbulence (ICMART) model where abrupt dissipation occurs through magnetic reconnections in a Poynting flux dominated jet (Zhang & Yan 2011); (ii) dissipation occurring within a fuzzy photosphere; the photosphere is specially invoked to explain the quasi-thermal shape of the spectrum. The process manifests itself in such a way that it can produce a non-thermal shape of the spectrum as well (Beloborodov 2017), (iii) gradual magnetic dissipation that occurs within the photosphere of a Poynting flux dominated jet (Beniamini & Giannios 2017) and (iv) Comptonization of soft corona photons off the electrons present in the outgoing relativistic ejecta (Titarchuk et al. 2012; Frontera et al. 2013). These models are designed to explain the spectral properties of the prompt emission of GRBs and are successful to a certain extent. Some prominent features like the evolution of the spectral parameters and the presence of correlations among GRB observables are not well understood and most of them remain unexplained within the framework of a single model.

Another crucial information that can be added to the existing plethora of observations of the prompt emission

like the spectral and timing properties, presence of afterglows, presence of associated supernovae etc, is the polarization of the prompt emission. Detection of polarization, therefore, provides an additional tool to test the theoretical models of the mechanism of GRB prompt emission. This, however, has remained a scarcely explored avenue due to the unavailability of dedicated polarimeters and reliable polarization measurements. The Cadmium Zinc Telluride Imager (CZTI) on board *AstroSat*, offers a new opportunity to reliably measure polarization of bright GRBs in the hard X-rays (Chattopadhyay et al. 2014; Vadawale et al. 2015; Chattopadhyay et al. 2017). The polarization expected from different models of prompt emission is not only different in magnitude but also in the expected pattern of temporal variability, depending on the emission mechanism, jet morphology and view geometry (see e.g. Covino & Gotz 2016). A study of the time variability characteristics is very important because bright GRBs whose spectra have been studied in great detail often found to have spectra deviating significantly from the standard Band function conventionally used to model the GRB spectra (Abdo et al. 2009; Izzo et al. 2012; Ackermann et al. 2010; Vianello et al. 2017; Wang et al. 2017).

GRB 171010A is a bright GRB and it presents an opportunity for a multi-pronged approach to understand the GRB prompt emission. It has been observed by both *Fermi* and *AstroSat*-CZTI. Afterglows in gamma-rays (*Fermi*/LAT), X-rays (*Swift*-XRT) and optical have been detected, and an associated supernova SN 2017htp has been found on the tenth day of the prompt emission. A redshift $z = 0.33$ has been measured spectroscopically by the *extended Public ESO Spectroscopic Survey for Transient Objects* (ePESSTO) optical observations (Kankare et al. 2017). We present here a comprehensive analysis of this GRB using the *Fermi* observation for spectral properties and attempt to relate the prompt spectral properties to the detection of variable high polarization using *AstroSat*-CZTI. We present a summary of the observations in Section 2. The *Fermi* light curves and spectra are constructed in various energy bands and time bins respectively and they are presented in Sections 2, 3 and 4. The polarization measurements in different time intervals and energies are presented in Section 6. We discuss our results and derive conclusions in Section 7. The cosmological parameters chosen were $\Omega_\lambda = 0.73$, $\Omega_m = 0.27$ and $H_0 = 70 \text{ km Mpc}^{-1} \text{ sec}^{-1}$ (Komatsu et al. 2009).

2. GRB 171010A

GRB 171010A triggered the *Fermi*-LAT and *Fermi*-GBM at 19:00:50.58 UT (T_0) on 2017 October 10

(Omodei et al. 2017; Poolakkil & Meegan 2017). The observed high peak flux generated an autonomous re-point request (*ARR*) in the GBM flight software and the *Fermi* telescope slewed to the GBM in-flight location. A target of opportunity observation was carried out by the *Niel Gehrels Swift Observatory* (Evans 2017) and the *Swift*-XRT localized the burst to $RA(J2000) : 66^{\circ}.58092$, and $Dec : -10^{\circ}.46325$ (D’Ai et al. 2017). *Swift*-XRT followed the burst for $\sim 2 \times 10^6 \text{ s}^1$. The prompt emission was also observed by *Konus-Wind* (Frederiks et al. 2017). The fluence observed in the *Fermi*-GBM 10 - 1000 keV band from $T_0 + 5.12 \text{ sec}$ to $T_0 + 151.55 \text{ s}$ is $(6.42 \pm 0.05) \times 10^{-4} \text{ erg cm}^{-2}$ (Poolakkil & Meegan 2017). Here T_0 is the trigger time in the *Fermi*-GBM. The first photon in LAT ($> 100 \text{ MeV}$) with a probability 0.9 of its association with the source is received at $\sim T_0 + 374 \text{ s}$ and has an energy $\sim 194 \text{ MeV}$ and a photon with energy close to 1 GeV (930 MeV) is detected at $\sim 404 \text{ s}$. The highest energy photon ($\sim 19 \text{ GeV}$) in the *Fermi*-LAT is detected at $\sim 2890 \text{ s}$. The rest frame energy of this photon is $\sim 25 \text{ GeV}$.

3. LIGHT CURVES

We examined the light curves of the GRB as obtained from all 12 NaI detectors and found that detectors n7, n8 and nb (using the usual naming conventions) have significant detections (source angles are $n7 : 69^{\circ}$, $n8 : 31^{\circ}$ and $nb : 40^{\circ}$). We have used data from all three detectors to examine the broad emission features of the GRB. For wide band temporal and spectral analysis, however, we chose n8 and nb, which have higher count rates than the other detectors and the angles made with the source direction for these two detectors are less than 50 degrees. The time scale used throughout this paper is relative to the *Fermi*-GBM trigger time *i.e.* $t = T - T_0$. Of the two BGO scintillation detectors, the detector BGO 1 (b1), which is positioned on the same side on the satellite as the selected NaI detectors, is chosen for further analysis.

The light curve is shown in Figure 1 and it shows two episodes of emission (a) beginning at $\sim -5 \text{ s}$ of the main burst and lasts up to $\sim 205 \text{ s}$ followed by a quiescent state when the emission level meets the background level and (b) the emission becomes active again after a short period at $\sim 246 \text{ s}$ and radiation from the burst is detected till $\sim 278 \text{ s}$. We name these emission phases as Episode 1 & 2. In Figure 1 we also show the light curve in the 100 - 400 keV region (the energy range of *AstroSat*-CZTI observations) and we use this light curve

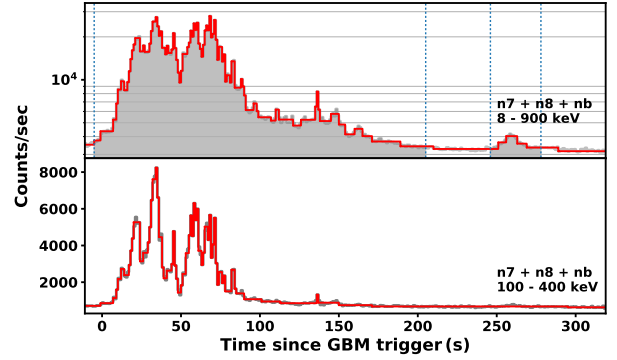


Figure 1. *Fermi*-GBM light curve of GRB 171010A obtained from three NaI detectors n7, n8 and nb.

Upper Panel: Log-scale light curve in the full energy range (8 - 900 keV), binned in 1 s intervals. The two emission episodes used for time-integrated spectral analysis (-5 s to 205 s , 246 s to 278 s) are shaded and demarcated with vertical dotted lines. The red envelope shows the Bayesian blocks representation of the light curve.

Lower panel: Linear-scale light curve and Bayesian blocks representation for the 100 - 400 keV energy range used in time-resolved spectral analysis.

to divide the data for time resolved spectral analysis. The blocks of constant rate (Bayesian blocks) are constructed from the light curves and over-plotted on the count rate light curves to show statistically significant changes in them (Scargle et al. 2013).

The light curves summed over the chosen GBM detectors (n8 and nb) in six different energy ranges are shown in Figure 2. The GRB has complex structure with multiple peaks and the high energy emission (above 1 MeV) is predominant till about 50 s as seen in the light curve for $> 1 \text{ MeV}$. Bayesian blocks are constructed from the light curves and over-plotted on the count rate.

4. SPECTRAL ANALYSIS

The burst is very bright and even with a signal to noise ratio of 50, we are able to construct more than 150 time bins. We created time bins, therefore, from the Bayesian blocks constructed from the light curve in the energy range 100 keV to 400 keV where CZTI is sensitive for polarization measurements. These bins (large number of Bayesian blocks) track significantly varying features in the lightcurve and will also be sufficient to give a substantial idea about the energetics of the burst. The spectra are reduced using *Fermi* Science tools soft-

¹ http://www.swift.ac.uk/xrt_curves/00020778/

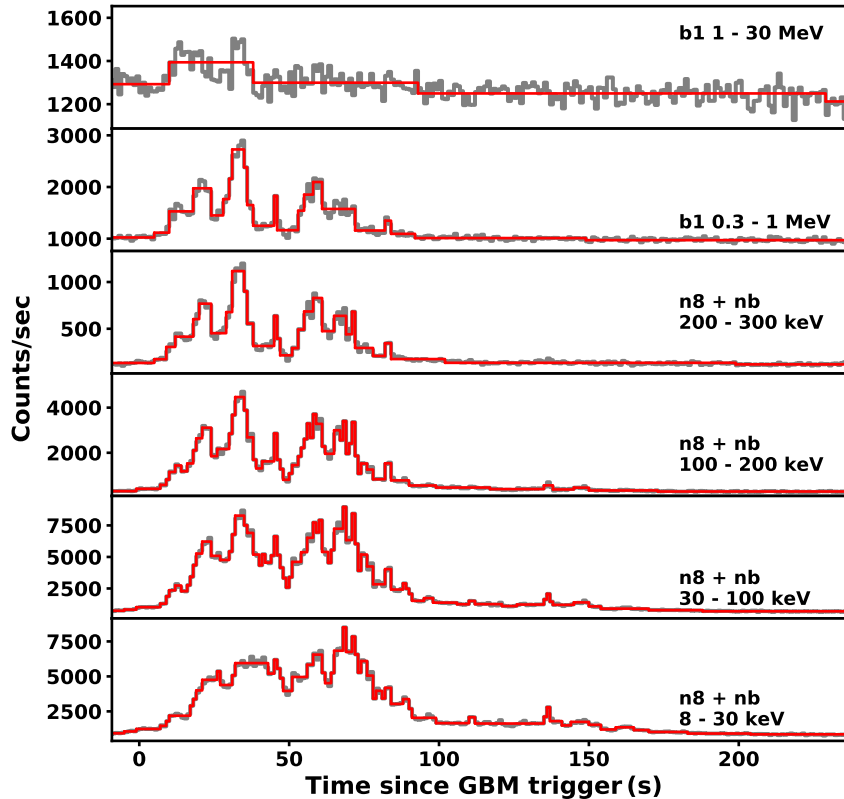


Figure 2. *Fermi*-GBM light curve of GRB 171010A in six different energy ranges, with Bayesian blocks over-plotted in red. At the highest energies (1 – 30 MeV, top panel), the emission is low after ~ 50 s.

ware *rmfit*² by standard methodology described in the tutorial³.

GRB prompt emission spectra generally show a typical shape described by the Band function (Band et al. 1993), however, for a number of bursts additional components are observed in the spectra such as quasi-thermal components modeled by blackbody function (Ryde 2005; Page et al. 2011; Guiriec et al. 2011; Basak & Rao 2015) or they show additional non-thermal components modeled by a power-law or a power-law with an exponential cut-off (Abdo et al. 2009; Ackermann et al. 2013). Additionally, for a few cases, spectra with a top-hat shape are also observed and modeled by a Band-function with an exponential roll-off at higher energies (Wang et al. 2017; Vianello et al. 2017).

² *Fermi* Science Tools, *rmfit*: <https://fermi.gsfc.nasa.gov/ssc/data/analysis/rmfit>

³ *Fermi* tutorial: https://fermi.gsfc.nasa.gov/ssc/data/analysis/scitools/rmfit_tutorial.html

The above models are driven by data and phenomenology. The physical models devised to explain the GRB prompt emission radiation have the synchrotron emission or the Compton scattering as the core processes. The synchrotron spectrum for a power-law distribution of electrons consists of power-laws joined at energies which depend upon cooling frequency (ν_c), minimum-injection frequency (ν_m) and absorption frequency (ν_a). The Comptonization models include inverse Compton scattering as a primary mechanism (Lazzati et al. 2000; Titarchuk et al. 2012). Comptonization signatures (*XSPEC grbcomp* model) have been detected for a set of GRBs observed by Burst and Transient Source Experiment (*BATSE*) on board *Compton Gamma Ray Observatory* (Frontera et al. 2013). The *grbcomp* model differs from the other Comptonization model: the Compton drag model. In the Compton drag model the single inverse Compton scatterings of thermal photons shape the spectrum, while in the *grbcomp* multiple Compton scatterings are assumed. Another major difference is that the scattering

is off the outflow which is sub-relativistic in case of `grbcomp` model, while relativistic in the Compton drag model.

We apply this prior knowledge of spectral shapes from the previous observations of GRBs to study GRB 171010A. The spectra are modeled by various

spectroscopic models available in *XSPEC* (Arnaud 1996). The statistics `pgstat` is used for optimization and testing the various models⁴. We start with the Band function, and use the other models based upon the residuals of the data and model fit. The functional form of the Band model used to fit the photon spectrum is given in Equation 1 (Band et al. 1993),

$$N_{\text{Band}}(E) = \begin{cases} K_B (E/100)^\alpha \exp(-E(2+\alpha)/E_p) & , E < E_b \\ K_B \{(\alpha - \beta) E_p / [100(2+\alpha)]\}^{(\alpha-\beta)} \exp(\beta - \alpha) (E/100)^\beta & , E \geq E_b \end{cases} \quad (1)$$

Other models include `blackbody`⁵ (BB) and a power law with two breaks (`bkn2pow`)⁶ to model the broad band spectrum.

$$N_{\text{bkn2pow}}(E) = \begin{cases} K E^{-\alpha_1} & , E \leq E_1 \\ K E_1^{\alpha_2 - \alpha_1} E^{-\alpha_2} & , E_1 \leq E \leq E_2 \\ K E_1^{\alpha_2 - \alpha_1} E_2^{\alpha_3 - \alpha_2} E^{-\alpha_3} & , E \geq E_3 \end{cases} \quad (2)$$

For the Comptonization model proposed by Titarchuk et al. 2012, *XSPEC* local model `grbcomp` is fit to the photon spectrum⁷. The pivotal parameters of this model are temperature of the seed blackbody spectrum (kT_s), the bulk outflow velocity of the thermal electrons (β), the electron temperature of the sub-relativistic outflow (kT_e), and the energy index of the Green's function with which the formerly Comptonized spectrum is convolved (α_b). Using the normalization of the `grbcomp` model, the apparent blackbody radius can be obtained. To avoid degeneracy in the parameters or the case when parameters are difficult to constrain, we froze some of the parameters.

To fit the spectra with synchrotron radiation model we implemented a table model for *XSPEC*. We assumed a population of electrons with a power-law energy distribution (as a result of acceleration) $dN/d\gamma \propto \gamma^{-p}$ for $\gamma > \gamma_m$, where γ_m is the minimum Lorentz factor of electrons. The cooling of electrons by synchrotron radiation is considered in slow and fast cooling regimes

depending on ratio between γ_m and the cooling Lorentz factor γ_c (Sari et al. 1998). We computed the resulting photon spectrum of population of electrons assuming that the average electron distribution at a given time is $dN/d\gamma \propto \gamma^{-2}$ for $\gamma_c < \gamma < \gamma_m$ and $dN/d\gamma \propto \gamma^{-p-1}$ for $\gamma > \gamma_m$ in fast cooling regime while $dN/d\gamma \propto \gamma^{-p}$ for $\gamma_m < \gamma < \gamma_c$ and $dN/d\gamma \propto \gamma^{-p-1}$ for $\gamma > \gamma_c$ in slow cooling regime. The synchrotron model is made of four free parameters: the ratio between characteristic Lorentz factors γ_m/γ_c , the peak energy of F_ν spectrum E_c which is simply the energy which corresponds to the cooling frequency, the power-law index of electrons distribution p and the normalization. We built the table model for the range of $0.1 \leq \gamma_m/\gamma_c \leq 100$ and $2 \leq p \leq 5$.

To fit the time integrated spectrum of Episode 1, we use the four models described above: (i) Band, (ii) Band + blackbody (BB), (iii) broken power law (`bkn2pow`), and (iv) the Comptonization model (`grbcomp`). The best fit parameters of the tested models are reported in Table 1. The νF_ν plots, along with the residuals, are shown in Figure 3 for the four models used. The Band fit shows deviations at lower energies signifying deviations from the power law that is used to model the spectra from the low energy threshold of 8 keV to the peak energy of the Band function (~ 150 keV). We have examined these residuals in detail by progressively raising the low energy threshold to 40 keV (greater than the energy in which the deviations are seen) and ex-

⁴ <https://heasarc.gsfc.nasa.gov/xanadu/xspec/manual/node293.html>

⁵ `blackbody` model: <https://heasarc.gsfc.nasa.gov/xanadu/xspec/manual/node136.html>

⁶ `bkn2pow` model: <https://heasarc.gsfc.nasa.gov/xanadu/xspec/manual/node141.html>

⁷ `grbcomp` model: <https://heasarc.nasa.gov/docs/xanadu/xspec/models/grbcomp.html>

trapolating the model to the low energies. The low energy features could still be seen. The presence of such an anomaly is found in previous studies (Tierney et al. 2013) and we conclude that a separate low energy feature in the spectra can exist. We included a blackbody (BB) along with the Band model for higher energies, but the residuals still show a systematic hump. We also tried another model for this feature of the spectrum: a power-law with two breaks (**bkn2pow** model). The **bkn2pow** model is preferable as the $\Delta pgstat$ is much less for the same number of parameters ($\Delta pgstat = 41$). The presence of a narrow residual hump also necessitate the need of a sharper break than a smooth blackbody curvature. This also hints that the break does not evolve much in time and thus, is not smeared out. The Comptonization model (**grbcomp**), however, gives the best fit for the time integrated spectrum of Episode 1. All the parameters of this model other than β , **fbflag** and $\log(A)$ were left free. The parameter β was frozen to the value 0.2 to ignore terms $O(\sim \beta^2)$ and **fbflag** was set to zero to include only the first order bulk Comptonization term. A value of 3.9 for γ shows deviation for the seed photons from the seed blackbody spectrum. However, during the time resolved spectral analysis as reported in the next subsection we kept it fixed to 3 to consider a blackbody spectrum for the seed photons.

The isotropic energy ($E_{\gamma,iso}$) is calculated in the cosmological frame of the GRB by integrating the observed energy spectrum over $1 \text{ keV}/(1+z)$ to $10 \text{ MeV}/(1+z)$. The tested models differ significantly only at low energies and yield similar $E_{\gamma,iso}$. We have $E_{\gamma,iso} = 2.2 \times 10^{53}$ erg for the best fit model **grbcomp**. The $\Gamma_0 - E_{\gamma,iso}$ correlation between the initial Lorentz factor and the isotropic energy can be used to estimate Γ_0 of the fireball ejecta (Liang et al. 2010). The estimated Γ_0 is 392^{+38}_{-34} . The errors are propagated from the normalization and slope of the correlation. The episode 2 could be spectrally well described by a simple power-law and the best fit power-law index is $1.90^{+0.07}_{-0.06}$ for **pgstat** 274 for 229 degrees of freedom.

4.1. Parameters evolution

We performed time resolved analysis to capture the variations in the spectral properties by dividing the data into time segments based on the Bayesian blocks made from the 100 - 400 keV light curve. We test the models that were used for the time-integrated analysis. The deviation from Band spectrum at low energies observed in the time-integrated spectrum is also present in the time-resolved bins, thus justifying the need to use more complex models than the simple Band function. We, however, find that the three additional models (Band+BB,

bknpwl, and **grbcomp**) represent the time resolved spectral data equally well. The evolution of the model parameters is shown in Figure 4. In *Fermi*-GBM, energy range 8-20 keV is divided into 12 energy channels and thus it provided sufficient data points to constrain the power-law or BB temperature whenever BB peak or low energy break falls well within these energy channels. In case of **bkn2pow**, the low energy index is very steep (~ -3) when the break energy E_1 found to be close to the lower edge of the detection band. For such cases, we froze the index to -3 to obtain constraints on the other parameters of the model. When we fit with the Band function, the peak energy E_p shows three pulse like structures in their temporal evolution and these can be identified as showing a hard to soft (HTS) evolution for peaks in the photon flux. The first structure in E_p (at ~ 10 s) can be associated with the enhancement seen in the >1 MeV flux (Figure 2, top panel). When the low energy feature is modeled using **bkn2pow**, almost all the peak energies fall below 200 keV. The variation in the low energy break (E_1) remains concentrated in a very narrow band (10 - 20 keV). The best fit parameters for all the models are presented in Table 5.

The evolution of the derived parameters of **grbcomp** model such as photospheric radius (R_{ph}) and bulk parameter (δ) is shown in Figure 6.

4.1.1. Distribution of parameters

Despite the fact that the best fit to the time integrated spectrum is the Comptonization model (**grbcomp**), we have tested the models (i) Band, (ii) **bkn2pow**, (iii) BB+Band and (iv) **grbcomp** for the time resolved spectra. The distribution of the parameters is presented in Figure 7 and are summarized here.

For the Band function, the low energy index α is distributed with a mean value -1 ($\sigma = 0.13$). The maximum value observed is -0.25 for a few time bins and in the other cases α remains mostly below -0.8 . The values of low energy index agree with what is typically observed for long GRBs ($\langle \alpha \rangle = -1$) which is, however, known to be harder than the synchrotron radiation in the fast cooling regime. The high energy index follows a bimodal distribution with a mean value of -2.7 ($\sigma = 0.3$) for the major chunk concentrated around $-3 < \beta < -2$ and can be interpreted as values normally observed for GRBs. The peak energy E_p is between 32 keV and 365 keV with a median ~ 140 ($\sigma = 83$) keV. Its distribution also shows a bimodal nature which reflects the evolution of E_p .

In the case of **bkn2pow**, we observed that when the lower break energy E_1 is near the lower edge of the detection band, the power-law index below E_1 is very

Table 1. The best fit parameters for the time integrated spectrum of GRB 171010A, Episode 1

| Model | | | | | | |
|-------------------|-------------------------|---------------------------|------------------------|------------------------|--------------------------|------------|
| Band | α | β | E_p (keV) | pgstat/dof | | |
| | $-1.15^{+0.01}_{-0.01}$ | $-2.40^{+0.03}_{-0.03}$ | 163^{+3}_{-3} | 2786/335 | | |
| BB+Band | α | β | E_p (keV) | kT_{BB} (keV) | pgstat/dof | |
| | $-0.75^{+0.04}_{-0.03}$ | $-2.40^{+0.04}_{-0.03}$ | $150.0^{+2.5}_{-2.6}$ | $5.8^{+0.1}_{-0.1}$ | 1465/333 | |
| bkn2pow | α_1 | α_2 | α_3 | E_1 (keV) | E_2 (keV) | pgstat/dof |
| | $0.48^{+0.06}_{-0.07}$ | $1.464^{+0.006}_{-0.005}$ | $2.33^{+0.02}_{-0.02}$ | $17.2^{+0.4}_{-0.4}$ | $132.7^{+2.3}_{-2.3}$ | 1421/333 |
| grbcomp | kT_s (keV) | kT_e (keV) | τ | α_b | R_{ph} (10^{10} cm) | pgstat/dof |
| | $4.8^{+0.5}_{-0.4}$ | 55^{+3}_{-3} | $4.15^{+0.18}_{-0.15}$ | $1.52^{+0.04}_{-0.04}$ | $8.0^{+2.2}_{-2.0}$ | 1281/332 |
| Synchrotron model | γ_m/γ_e | E_c (keV) | p | pgstat/dof | | |
| | $4.06^{+0.03}_{-0.08}$ | $21.6^{+0.2}_{-0.4}$ | > 4.82 | 2520/335 | | |

steep. This is expected because there are only a few channels here and the fit probably gives an unphysical result. We thus fixed the values to -3 as they are difficult to constrain by the fits and also hamper the overall fitting process. Note that **bkn2pow** model is defined with an *a-priori* negative sign with it and we have to be cautious while comparing it with the Band function where the indices are defined without a negative sign. For the purpose of comparison we will explicitly reverse the signs of the **bkn2pow** indices. The mean value of $-\alpha_1$ is ~ 0.3 ($\sigma = 0.65$). Here, we have ignored values > 1.5 as they form another part of the bimodal distribution with low E_1 , during the time when E_1 is near the lower edge of the GBM energy band. The mean value of $-\alpha_2$ is ~ -1.4 ($\sigma = 0.22$). This forms the second power law from E_1 to E_2 . The third segment of the emission has power law index $-\alpha_3$ with a mean of ~ -2.6 ($\sigma = 0.23$). The low energy break E_1 has a mean ~ 16 ($\sigma = 2.3$) keV and it falls in a narrow range of 11 to 20 keV. The mean E_2 is ~ 140 ($\sigma = 32$) keV, comparable to the mean of Band function peak energy with a uni-modal distribution. The E_2 values are concentrated in the range 93 to 350 keV.

When a blackbody is added, the fits have an improved statistics compared to the Band function throughout the burst (see Figure 5). The blackbody temperature vary between 4 – 10 keV with a median of ~ 6.3 ($\sigma = 1.12$) keV. The α distribution has harder values, while E_p and β are similar to the distributions of their counterparts in the Band function. The presence of blackbody does not seem to move the peak energies significantly, albeit an upward shift is noticeable. In the **grbcomp** model, the average temperature of the seed photons was 6.8 ($\sigma = 0.8$) keV. The electron temperature kT_e was found to be 55 ($\sigma = 21$) keV. We derived the photospheric radius from the normalization of the model. We found the photospheric radius $\sim 10^{11}$ cm. The **grbcomp** model parameters are reasonable and a photospheric ra-

dus of 10^{11} cm is consistent with its predictions (Frontera et al. 2013).

4.1.2. Correlations of parameters

We explore two parameter correlations and present the graphs in Figure 8.

(i) kT_{BB} vs E_p : Thermal components observed in a set of bright *Fermi* single pulse GRBs are correlated to the peak of non-thermal emission (Burgess et al. 2014a). The exponent of the power-law relation ($E_p \propto T^q$) indicates the position of the photosphere if it is in the coasting phase or acceleration phase. The jet is dominated by magnetic fields when q is 2 and baryonic if q is nearly 1. However, these results were found on GRBs with single pulses and for GRBs made up of overlapping pulses such criteria may not be valid. For GRB 171010A a positive correlation ($E_p \propto T^{2.2}$) between E_p and kT_{BB} is found with a log linear Pearson correlation coefficient of 0.81, p-value $\sim 10^{-15}$. The index points out, therefore, a magnetically dominated jet with photosphere below the saturation radius. We will discuss this result coupled with the polarization results in Section 7. The peak energy from Band function and BB + Band function are also found to be correlated, $E_{p, Band} \propto E_{p, BB+Band}^{1.2}$.

(ii) *Correlations among grbcomp parameters*: Correlations between **grbcomp** model parameters and other model parameters are reported in Frontera et al. (2013). We found a strong correlation between peak energy of the Band function and the bulk parameter (δ) with log linear Pearson coefficient and p-value $r(p)$ of -0.68 ($\sim 10^{-9}$). The seed photon temperature kT_{BB} and photospheric radius R_{ph} are uncorrelated contrary to a strong anti-correlation reported in Frontera et al. 2013. The seed blackbody temperature and the electron temperature are not correlated, consistent with the predictions of **grbcomp** model. The parameter kT_e and peak energy of BB + Band model are correlated, with $kT_e \propto E_{p, BB+Band}^1$.

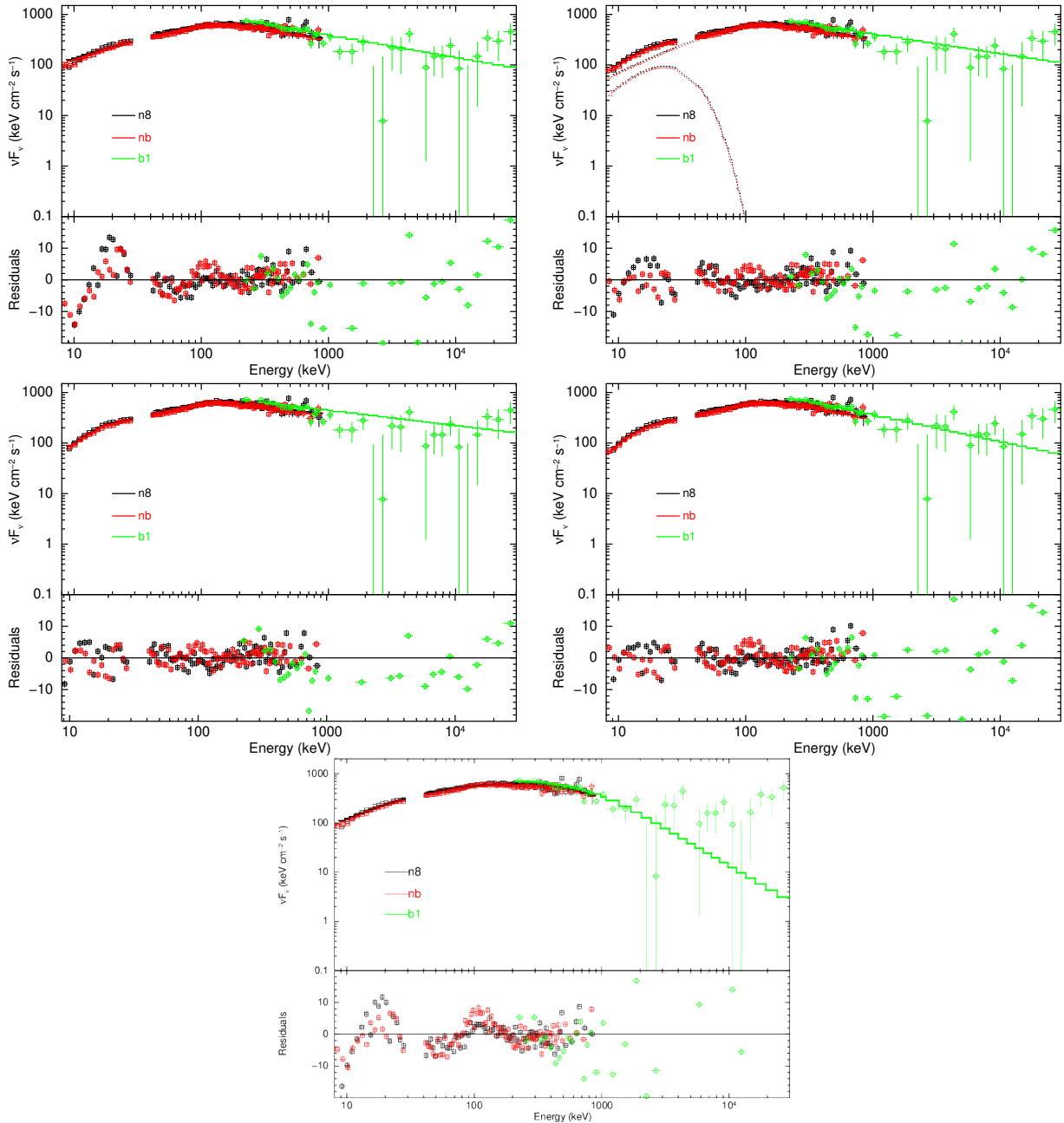


Figure 3. The time integrated νF_ν plot of Episode 1 of GRB 171010A (-5 s to 246 s) along with the best fit models. Residuals to the fit are shown in the bottom panels. The Band model (top left) shows a low energy feature and can be either modeled by blackbody (top right) or by adding another powerlaw at the low energy (middle left). The best fit model is the Comptonization model `grbcomp` (middle right). The synchrotron model is shown in bottom panel.

5. AFTERGLOWS

We have analyzed the afterglow data of GRB 171010A in gamma-rays (*Fermi*-LAT) and X-rays (*Swift*-XRT) and the results are shown in Figure 9 and 10.

5.1. γ -ray afterglows

A 12° region of interest (ROI) was selected around the refined *Swift*-XRT coordinates and an angle of 100° between the GRB direction and *Fermi* zenith was selected

based on the navigation plots. The zenith cut is applied to reduce the contamination from γ -rays of Earth albedo. Transient event class and its instrument response function `P8R2_TRANSIENT020E_V6` is used as it is appropriate for GRB durations. Details about LAT analysis methods and procedures can be found in the *Fermi*-LAT GRB catalog (Ackermann et al. 2013).

A simple power-law temporal decay is observed for the LAT light curve with a hint of momentary increase or

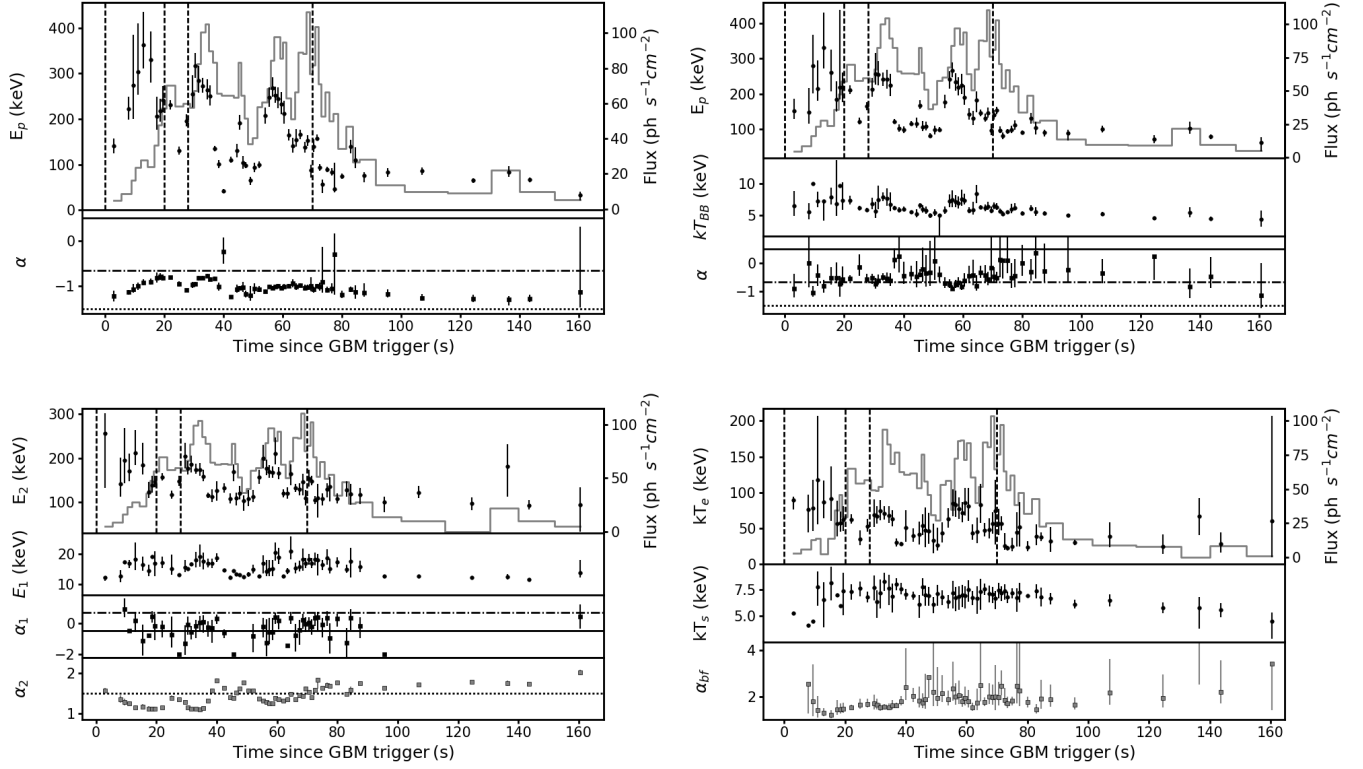


Figure 4. *Upper Left* : The evolution of peak energy and the low energy spectral index of the Band model fit to time resolved spectra. The low energy spectral indices lie between fast and slow cooling limits of synchrotron radiation (indicated by dotted line and dot-dashed line, respectively). **Intervals used for polarization measurement are segregated by vertical dotted lines, to guide the eye.** The photon flux is shown as a grey histogram (right hand side scale). *Upper Right*: The evolution of peak energy, blackbody temperature and low energy index when the low energy anomaly seen in the Band function fit is modeled by an additional blackbody. Low energy indices are now above the slow cooling limit, but below the limit of jitter radiation (black solid line). *Lower Left*: The Evolution of two break energies and indices for a broken power law fit. The index $-\alpha_2$ in this case shifts closer to the fast cooling line or even softer than this limit. The energy index α_1 below the low energy break is harder with a median value 1/3. The break energy is also low and falls in the range between 15 - 25 keV. *Bottom Right* : Evolution of electron temperature, seed photon temperature and high energy index α_{br} of the Comptonization model `grbcomp`.

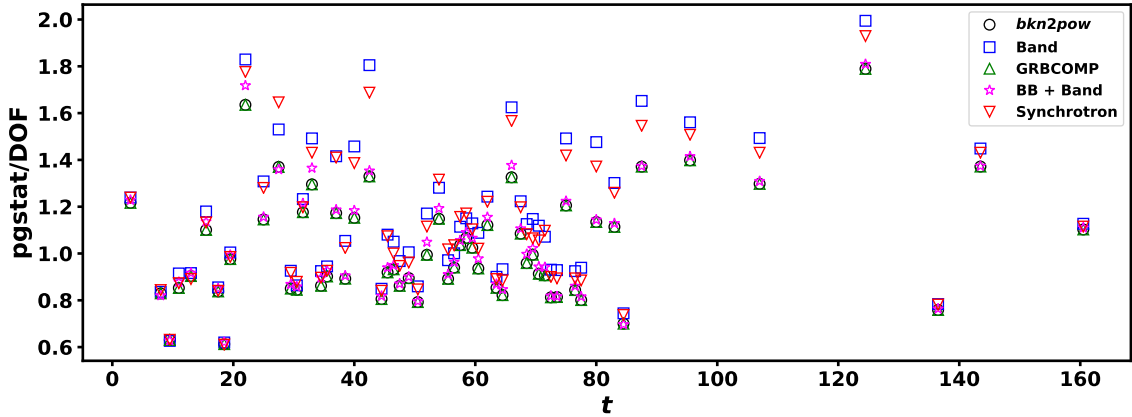


Figure 5. The variation of the statistic `pgstat` with time. A low energy break is preferable in almost all the bins. All three models: `BB+Band`, `bkn2pow`, `synchrotron` and `grbcomp` have comparable `pgstat` values and provide acceptable fits to the data in the time-resolved analysis. However, in time-averaged analysis, the `grbcomp` model provides the best fit.

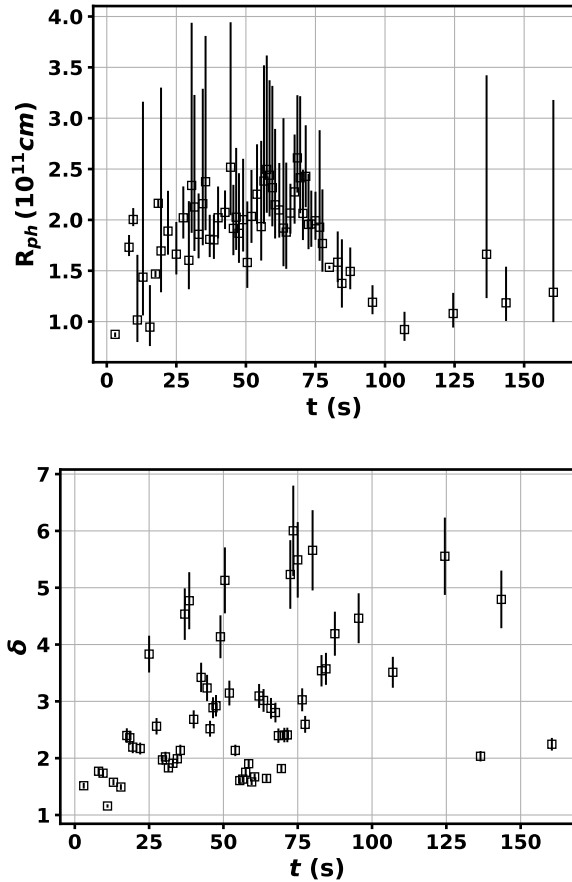


Figure 6. The evolution of the photospheric radius (upper panel) and the bulk parameter (lower panel) obtained from the `grbcomp` model.

steady emission in both energy and photon fluxes during the first and second time bins: 346 – 514 s & 514 – 635 s. The LAT photon flux varies with time as a power law with an index -1.56 ± 0.40 and the energy flux varies as a power law with an index -1.37 ± 0.45 . The photon index of LAT-HE is $\Gamma_L = -2.0 \pm 0.1$ from a spectral fit obtained by fitting the first 10^5 sec data. This gives spectral index $\beta_L = \Gamma_L + 1$ to be -1.0 ± 0.1 . The time resolved spectra do not show variation in the photon index in the first four bins.

In the external shock model, for $\nu > \max\{\nu_m, \nu_c\}$ which is generally true for reasonable shock parameters we can derive the power law index of the shocked electrons by $f_\nu \propto \nu^{-p/2}$. We have synchrotron energy flux $f_L \propto \nu^{-\beta_L} t^{-\alpha_L}$ (see the LAT lightcurve in Figure 9). We found $\alpha_L = 1.37 \pm 0.45$ and $\beta_L = 1.0 \pm 0.1$. The value of β_L gives us $p = 2.0 \pm 0.2$. Thus, the power-law index for the energy flux decay can be predicted by using $f_L \propto t^{(2-3p)/4}$. The calculated value of α_L is -1.0 ± 0.2 , which agrees well with the observed

value of -1.37 ± 0.45 . Hence, we can conclude that for GRB 171010A, the LAT high energy afterglows are formed in an external forward shock.

For the thin shell case in a homogeneous medium and assuming that the peak of the LAT afterglow (t_p) occurs either before or in the second time bin gives $t_p < 530$ s and we can constrain the initial Lorentz factor (Γ_0) of the GRB jet (see *e.g.* Sari & Piran 1999, Molinari et al. 2007) using

$$\Gamma_0 > 193(n\eta)^{-1/8} \times \left(\frac{E_{\gamma,52}}{t_{p,z,2}^3} \right)^{1/8} \quad (3)$$

where m_p is the mass of proton, η is the radiation efficiency, t_p is the time when afterglow peaks, $E_{\gamma,52}$ is the k corrected rest frame energy of the GRB in the 1 – 10,000 keV band. For a typical density $n = 0.1 \text{ cm}^{-3}$ of homogeneous ambient medium and $\eta = 0.5$, we can constrain the initial Lorentz factor $\Gamma_0 > 330$. This limit is consistent with Γ_0 found in Section 4 from $\Gamma_0 - E_{\gamma, iso}$ correlation.

The photon index hardens in the 2150 – 6650 s time bin and the flux also seems to deviate from the power law fit. This hints at a contribution from an inverse Compton component. The highest energy photon with a rest frame energy of $\sim 25 \text{ GeV}$ is also observed during this interval.

5.2. X-ray afterglows

The primary goal of the *Swift* satellite is to detect GRBs and observe the afterglows in X-ray and optical wavelengths. If a GRB is not detected by *Swift* but is detected by some other mission (like *Fermi* etc.), *target of opportunity* (ToO) mode observations can be initiated in *Swift* for very bright bursts. For such bursts the prompt phase is missed by *Swift* and afterglow observations are also inevitably delayed. However, the detection of X-ray afterglows with *Swift*-XRT not only allows us to study the delayed afterglow emissions but also to precisely localize the GRB for further ground and space based observations at longer wavelengths. The X-ray afterglow of GRB 171010A was observed by *Swift* ~ 24300 s (~ 0.3 days) after the burst. We have used the XRT products and lightcurves from the XRT online repository⁸ to study the light curve and spectral characteristics. The statistically preferred fit to the count rate light curve in the 0.3 – 10 keV band has three power-law segments with two breaks. The temporal power-law indices and the break times in the light curve, as given in the GRB online repository, are listed in Table 3. The data are also

⁸ http://www.swift.ac.uk/xrt_products/index.php

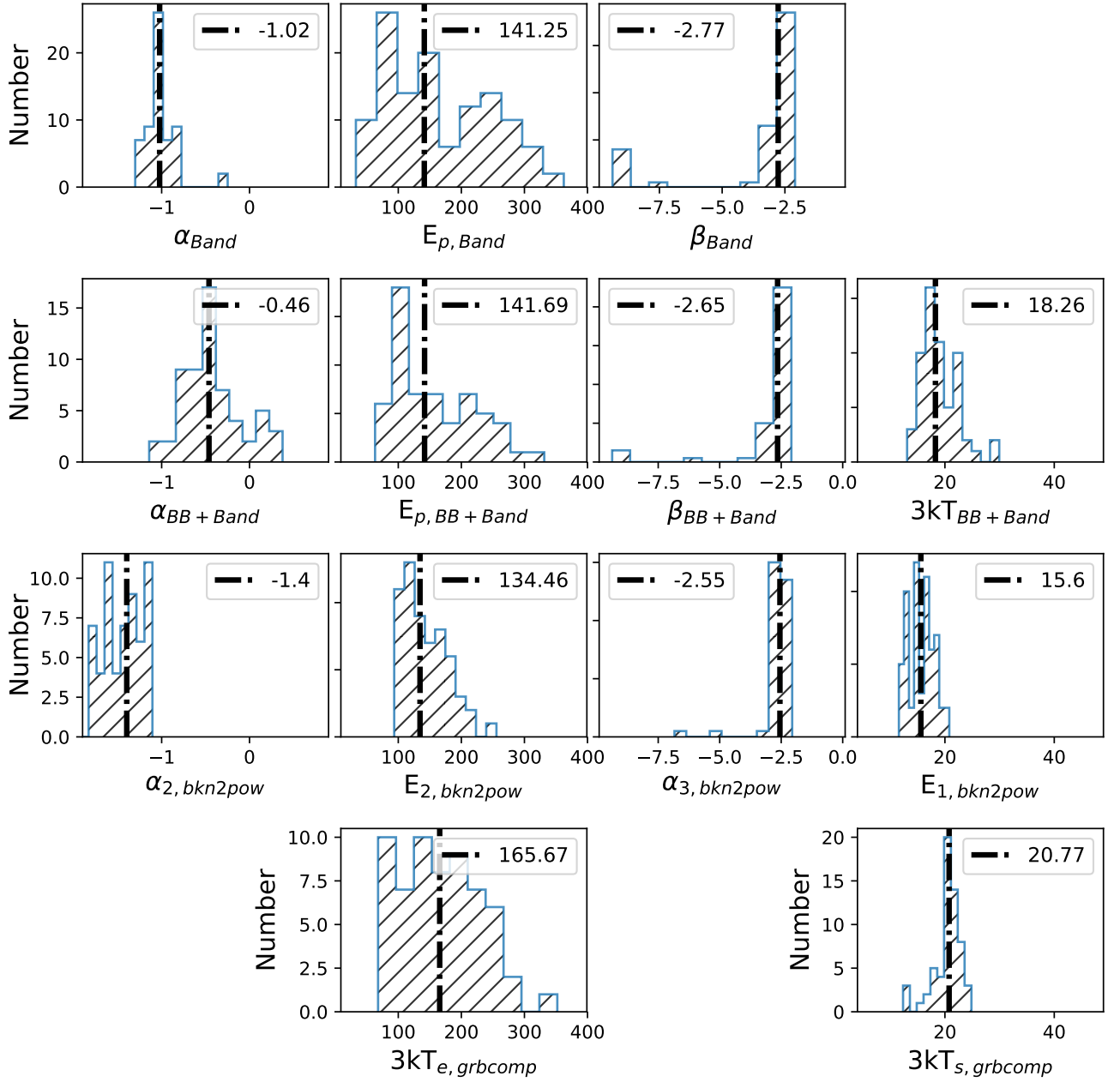


Figure 7. The distributions of best-fit parameters for **Band**, **bkn2pow** and **grbcomp** models. Each histogram consists of ten bins between minimum and maximum values. Thick vertical dot-dashed lines represent the median of the observed distribution of the parameters.

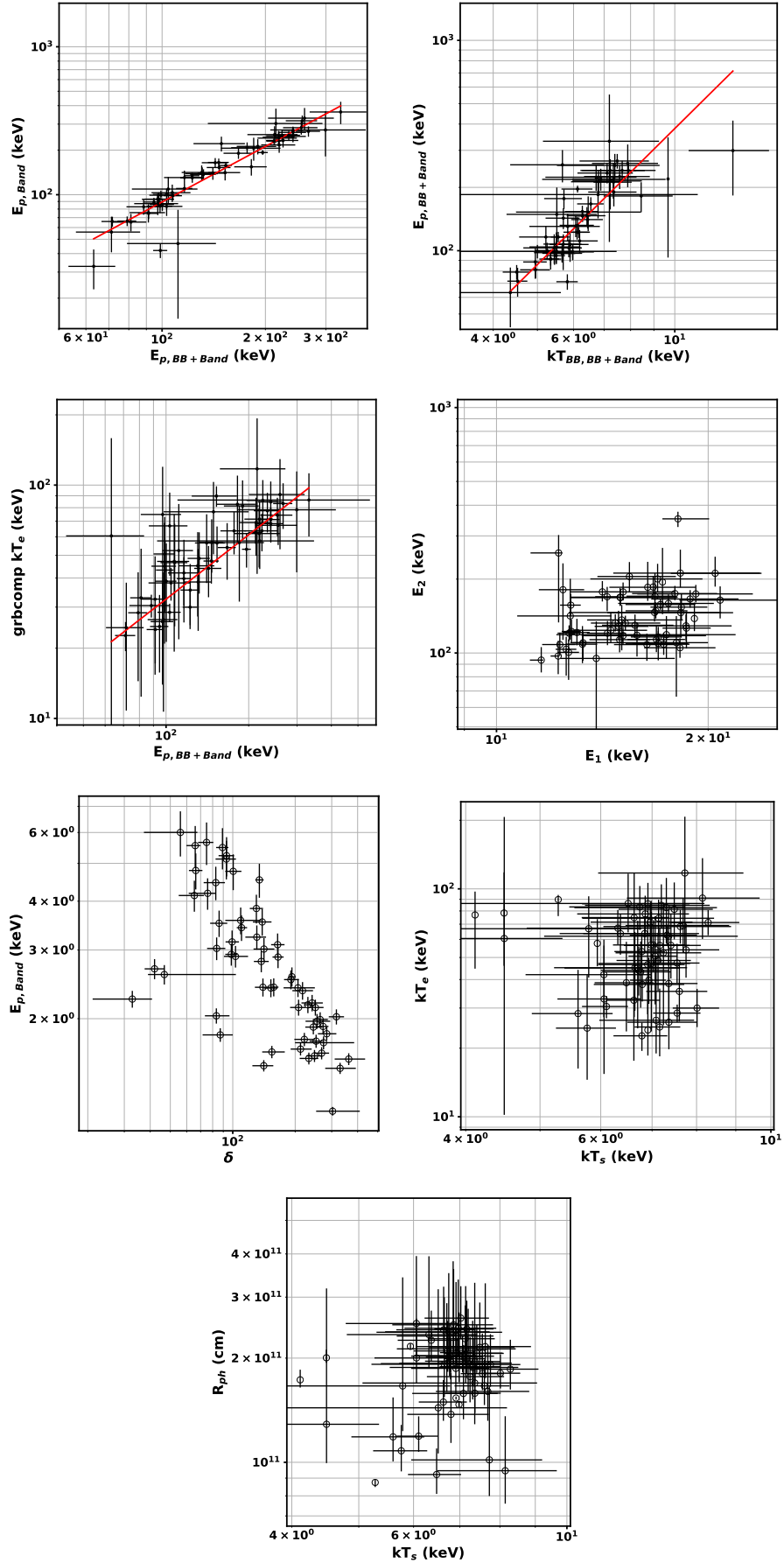


Figure 8. Correlations obtained for various model parameters and derived parameters.

consistent with 3 breaks (Table 3). The light curve with three breaks resembles the canonical GRB light curves observed in XRT (Zhang et al. 2006; Nousek et al. 2006). We have analysed the XRT spectral data and generated the energy flux light curve shown in Figure 10. The flux light curve in the 0.3 - 10 keV energy band is fit with a single powerlaw and a broken powerlaw with a single break at time t_b . The best fit single powerlaw shows a decay index of $f_X \propto t^{-1.44 \pm 0.03}$, while in the broken powerlaw the pre- and post-break decay indices are 1.29 ± 0.05 and 1.97 ± 0.24 respectively with the break at $t_b = (3.37 \pm 1.03) \times 10^5$ s. These values are consistent with the fits for the count rate light curves given in Table 3.

We name the two segments of the light curve with three breaks as phase 1 (see Table 3): before $t_{b,2}$ and phase 2: after $t_{b,2}$. The phase 1 is subjectively divided into 3 time bins to track the evolution of spectral parameters during this phase. The phase 2 is also divided at the $t_{b,3}$ for inspecting the spectral change with the apparent rise in the light curve after this point.

We froze the equivalent hydrogen column density (n_H) to its Galactic value (Willingale et al. 2013). Another absorption model *tbabs* in *XSPEC* is used to model intrinsic absorption and n_H corresponding to it is frozen to the value obtained from the time integrated fit. A simple power law fits the spectrum for both the phases.

The photon index in the XRT band is found to be $\Gamma_X = -1.9 \pm 0.1$ for phase 1 and $\Gamma_X = -1.7_{-0.6}^{+0.3}$ for phase 2. The evolution of energy flux in 0.3 - 10 keV and the photon index are shown in Figure 10. Similar to LAT, it also predicts $p \sim 2$ when both ν_m and ν_c evolve to energies that lie below the XRT band. If we consider $p \sim 2.2$ (See e.g. Zhang et al. 2006, Nousek et al. 2006) which will be nearly consistent with the p inferred from LAT afterglow and also near to XRT-afterglow value. Thus for the late time decay we have $\alpha_X \sim -1.15$. When the light curve is modeled by a broken power-law, we get $f_X \propto t^{-1.29 \pm 0.05}$ before the break and $f_X \propto t^{-1.97 \pm 0.24}$, thereafter. Therefore, predicted $\alpha_X \sim -1.15$ is nearly consistent with $\alpha_X \sim 1.29 \pm 0.05$ (three times the error bar). The α_X before and after the break are consistent with the late time decay in the external shock model. And, the break observed can be identified as a jet break ($t_{break} = 3.4 \times 10^5$ s) and used for finding the opening angle (θ_j) of the jet as given by Eq. 4 (Frail et al. 2001). However, an achromatic break at all wavelengths in the lightcurves is required to claim it as a jet break. The absence of a break till the last data point observed in *XRT* can also be utilized to put a lower limit on the jet break (see for example Wang et al. 2018). So any break before corresponding to last data point in XRT will also respect that limit because for a given initial Lorentz factor (Γ_0) the jet break will occur later for a wider jet.

$$\theta_j \approx 0.057 \left(\frac{t_j}{86,400 \text{ s}} \right)^{3/8} \left(\frac{1+z}{2} \right)^{-3/8} \left(\frac{E_{iso}}{10^{53} \text{ erg}} \right)^{-1/8} \left(\frac{\eta}{0.2} \right)^{1/8} \left(\frac{n}{0.1 \text{ cm}^{-3}} \right)^{1/8} \quad (4)$$

We get $\theta_j = 0.11 \text{ rad}$ ($= 6.3^\circ$) by using eq. 4. The beaming angle can be estimated by using Lorentz factor Γ_0 using $\theta_{beam} = 1/\Gamma_0$. For $\Gamma_0 = 330$, we have $\theta_{beam} = 0.003 \text{ rad}$ ($= 0.17^\circ$). Thus, we have a wide bright jet with a narrow beaming angle. The Lorentz factor estimated above is for the final merged shells propagating to the circum-burst medium (CBM) and forming an external shock. The Lorentz factor for individual shells can even be higher than our estimate. The jet energy corrected for collimation is $1.37 \times 10^{51} \text{ erg}$.

6. POLARIZATION MEASUREMENTS

GRB 171010A is one of the brightest GRBs detected in CZTI with an observed fluence $> 10^{-4} \text{ erg/cm}^2$. This makes the GRB one of potential candidates for polarization measurement. CZTI works as a Compton polarimeter where polarization is estimated from the azimuthal angle distribution of the Compton scattering events be-

tween the CZTI pixels at energies beyond 100 keV. Polarization measurement capability of CZTI has been demonstrated experimentally during its ground calibration (Chattopadhyay et al. 2014; Vadawale et al. 2015). First on board verification of its X-ray polarimetry measurement capability came with the detection of high polarization in Crab in 100 - 380 keV (Vadawale et al. 2017). Crab was observed for ~ 800 ks in two years after its launch and this was statistically the most significant polarization measurement till date in hard X-rays. Polarimetric sensitivity of CZTI for off-axis GRBs is expected to be less than that for ON-axis sources (e.g. Crab), but the high signal to background ratio for GRBs and availability of pre-GRB and post-GRB background makes CZTI equally sensitive to polarization measurements of GRBs. Recently, we reported systematic polarization measurement for 11 GRBs, with $\sim 3\sigma$ detection for 5 GRBs and $\sim 2\sigma$ detection for 1 GRB,

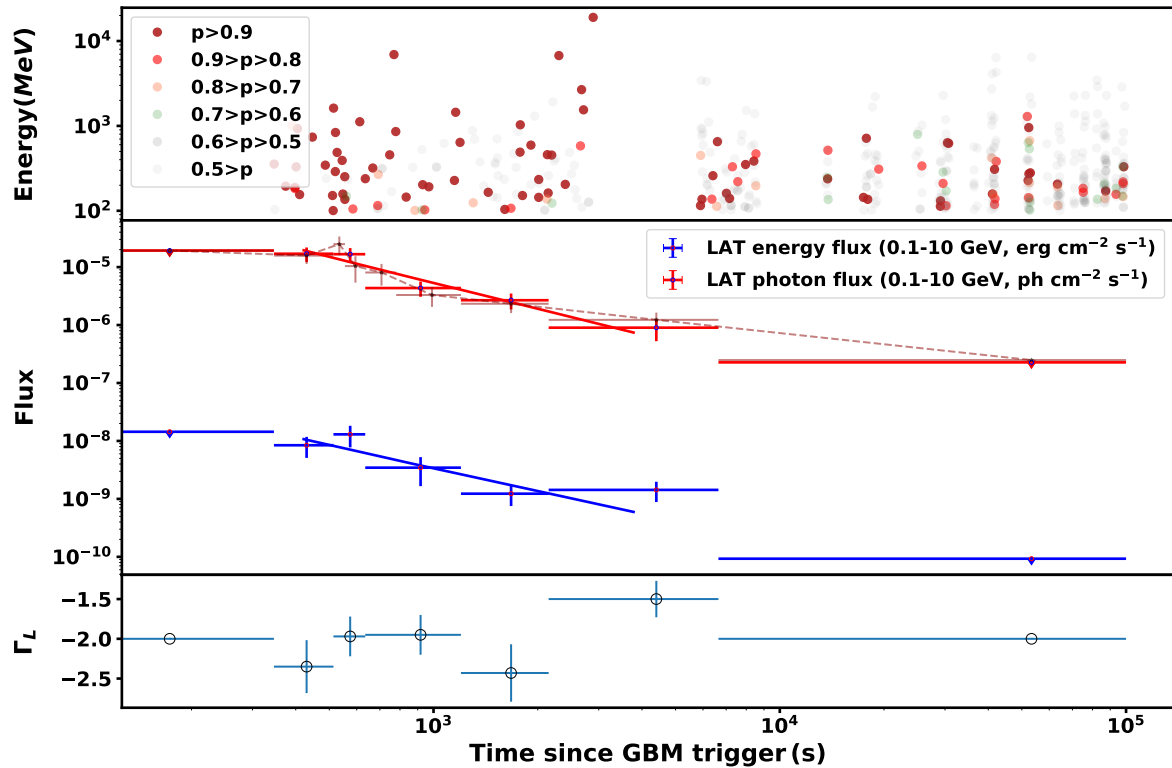


Figure 9. *Top panel:* Energies of individual *Fermi*-LAT photons (> 100 MeV), detected more than 345 s after the trigger. The color and transparency of circles depend on the probability (p) of their association with source. *Middle panel:* *Fermi*-LAT photon and energy fluxes in 0.1 — 10 GeV range. The photon index in the first time bin was fixed to -2 to get an upper limit on the fluxes. The dashed curve in the background shows the evolution of the LAT photon flux assuming a constant photon index, -2 . The photon flux rises fast initially, peaks at ~ 530 s, and then declines. This flux peak was used to obtain a lower limit on the Lorentz factor of the ejecta (§4). *Bottom panel:* Photon indices for *Fermi*/LAT in the 0.1 — 10 GeV range.

and upper limit estimation for the remaining 5 GRBs. GRB 171010A is a bright GRB registering around ~ 2000 Compton events in CZTI. It is the second brightest GRB in terms of number of Compton events after GRB 160821A, and therefore is a potential candidate for polarization analysis.

The details of the method of polarization measurement of GRBs with CZTI can be found in Chattopadhyay et al. (2017). Here we briefly describe the different steps involved in the analysis procedure.

- The first step is to identify and select the valid Compton events. We select the double pixel events during the prompt emission by identifying events happening within a $40 \mu\text{s}$ time window. The double pixel events are then filtered against various Compton kinematics criteria to finally obtain the Compton scattered events.

- The selection of Compton events is confined within the 3×3 pixel block of CZTI modules, which results in an 8 bin azimuthal scattering angle distribution. We compute the azimuthal scattering angles for events during both the GRB prompt emission and the background before and after the prompt emission. The combined pre and post-GRB azimuthal distribution is used for background subtraction to finally obtain the azimuthal distribution for the GRB.

- The background corrected prompt emission azimuthal distribution shows some modulation due to (a) asymmetry in the solid angles subtended by the edge and the corner pixels to the central scattering pixel, and (b) the off-axis viewing angle of the burst. These two factors are corrected by normalizing the azimuthal angle distribution with a simulated distribution for the same GRB spec-

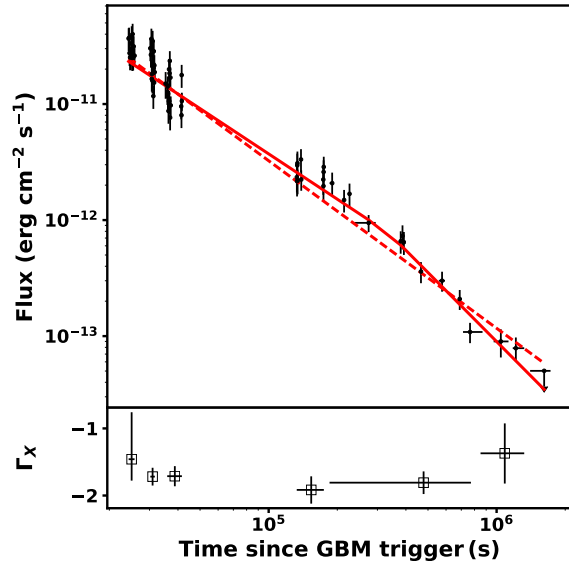


Figure 10. *Swift*-XRT energy flux in the range 0.3 - 10 keV (upper panel). A single power law fit (red dotted line) to the flux gives $f_X \propto t^{-1.44 \pm 0.03}$. When a break is introduced at t_b (red solid line), the powerlaw indices are 1.29 ± 0.05 and 1.97 ± 0.24 before and after the break, respectively. The break observed is at $(3.37 \pm 1.03) \times 10^5$ s. The photon indices for the *Swift*-XRT spectra are shown in the bottom panel.

tra at the same off-axis angle assuming the GRB is completely unpolarized. The simulation is performed in Geant4 with a full mass model of CZTI and *AstroSat*.

- We fit background and geometry corrected azimuthal angle distribution using MCMC simulation to estimate the modulation factor and polarization angle (in CZTI plane). This is followed up by detailed statistical tests to determine whether the GRB is truly polarized or not. This is an important step, particularly because, there can be systematic effects which can produce significant modulation in the azimuthal angle distribution even for completely unpolarized photons. These effects are even more prominent in cases where the GRB is not very bright.
- If the statistical tests suggest that the GRB is truly polarized, we estimate the polarization fraction by normalizing the fitted modulation factor with μ_{100} , which is the modulation factor for 100% polarized photons, obtained by simulating the GRB simulated in Geant4 with the *AstroSat* mass model. If the GRB is found to be unpolarized, we estimate the upper limit of polarization (see Chattopadhyay et al. (2017)).

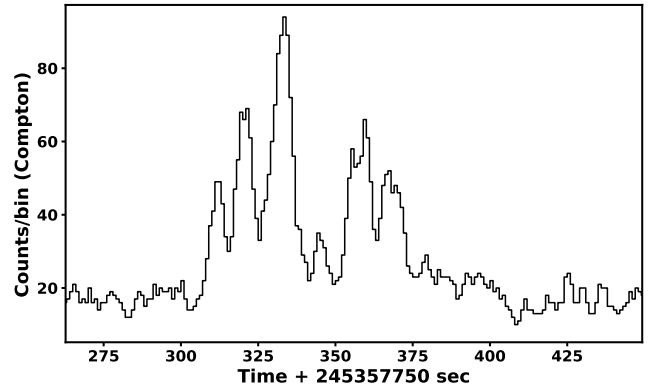


Figure 11. Observed Compton event light curve for GRB 171010A in 100 — 300 keV band with 1 second binning. The events in the time interval between 300—370 seconds in the light curve are used for polarization analysis.

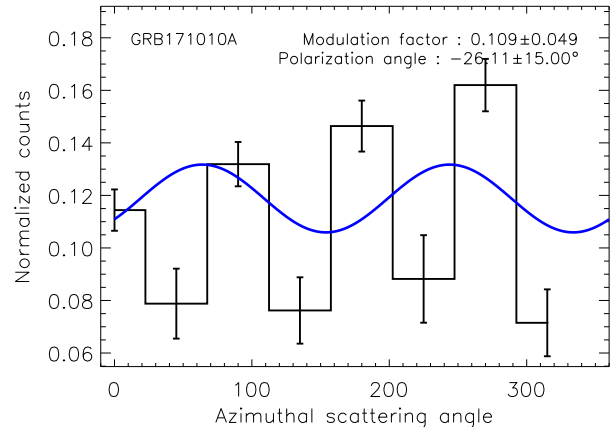


Figure 12. The background subtracted and geometry corrected modulation curve for GRB 171010A in 100 — 300 keV. The blue solid line is the sinusoidal fit to the modulation curve. We find no clear sinusoidal variation in the azimuthal angle distribution.

Figure 11 shows the light curve of GRB 171010A in Compton events in 100 — 300 keV. The burst is clearly seen in Compton events. We used a total of 747 seconds of background before and after the burst for the final background estimation. After background subtraction, the number of Compton events during the prompt emission is found to be ~ 2000 . Figure 12 shows the modulation curve in the 100 — 300 keV band following background subtraction and geometry correction as discussed in the last section. We do not see any clear sinusoidal modulation in the azimuthal angle distribution. Figure 13 shows the corresponding contour plot for GRB 171010A. Both polarization fraction and angle are poorly constrained signifying that the burst is

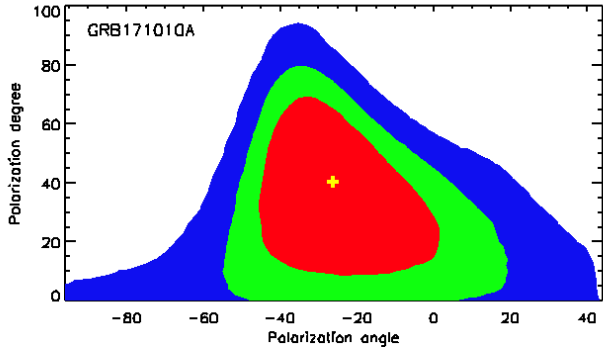


Figure 13. Contour plot of polarization angle and fraction for GRB 171010A in 100 — 300 keV as obtained from the MCMC method. The red, green and blue represent the 68 %, 90 % and 99 % confidence levels respectively.

either unpolarized or polarization fraction is below the sensitivity level of CZTI.

In order to verify this we measure Bayes factor for sinusoidal (for polarized photons) and constant model (unpolarized photons) by utilizing ‘Thermodynamic Integration’ method on the MCMC parameter space (for details refer to Chattopadhyay et al. (2017)). This yields a value less than 2 which is assumed to be the threshold value of Bayes factor for claiming detection of polarization. We therefore estimate the upper limit of polarization for GRB 171010A which is done in two steps. First step involves estimation of polarization detection threshold (P_{thr}) by limiting the probability of false detection (to 0.05 for $\sim 2\sigma$ or 0.01 for $\sim 3\sigma$). The false polarization detection probability is estimated by simulating GRB 171010A for the observed number of Compton and background events with 100 % unpolarized photons. The second step involves measurement of the probability of detection of polarization such that probability of detection of a certain level of polarization (P_{upper}) being greater than the polarization detection threshold (P_{thr}) is ≥ 0.5 (see Chattopadhyay et al. (2017) for more details). The 2σ upper limit (5 % of false detection probability) for GRB 171010A is found to be $\sim 42\%$. It is to be noted that in the sample of bursts used for polarization analysis in Chattopadhyay et al. (2017), GRB 160821A was found to possess maximum number of Compton events (~ 2500). The next brightest burst was GRB 160623A with ~ 1400 Compton events. We estimated $\sim 50\%$ polarization at $> 3\sigma$ detection significance for GRB 160821A. In comparison, GRB 171010A is found to have ~ 2000 Compton events. The GRB is detected at an off-axis angle of 55° . We expect CZTI to have significant polarmetric sensitivity at such off-axis angles. Therefore, polarization for this GRB should be detected at a significant detection level provided the GRB is at

least $\sim 50\%$ polarized. This is consistent to our estimation of 2σ polarization upper limit of $\sim 42\%$.

This is an interesting result considering the fact that the spectral analysis suggests the time integrated peak energy for all the models is less than 200 keV which falls within the energy range of polarization analysis. Therefore, in order to see the variation of polarization below and above the peak energy, we estimate polarization in two different energy ranges — 100 — 200 keV and 200 — 300 keV (see Figure 14). There is no clear modulation at the lower energies, whereas we see a sinusoidal variation in the modulation curve in 200 — 300 keV, which is beyond the peak energy of the GRB. However, it is to be noted that the Bayes factors for both the energy ranges are less than 2 signifying that there is no firm detection of polarization. The modulation at higher energies, therefore, is just a hint of polarization, which is still an interesting result.

One major difference between GRB 160821A (or GRB 160802A, GRB 160910A (Chattopadhyay et al. 2017)) and GRB 171010A, is that the later lasts longer and has multiple pulses. We also see significant variation of peak energy with time (see Figure 4). These pulses might exhibit different polarization signatures resulting in a net zero or low polarization when integrated in time. We therefore divided the whole burst in 3 different time intervals — 0 — 20 seconds, 20 — 28 seconds and 28 — 70 seconds, where ‘0’ is the onset of the burst. Since we have already seen a hint of polarization signature in 200 — 300 keV, we further divided the signals in 100 — 200 keV and 200 — 300 keV. Figure 15 shows the variation of polarization fraction (middle panel), and polarization angle (bottom panel) in three time intervals for 100 — 200 keV (left) and 200 — 300 keV (right). The errors in polarization angle in the first two intervals in both the energy ranges are quite large with no significant modulation in azimuthal angle distribution consistent to being unpolarized. This is independently verified with the estimation of low values of Bayes factor. The third interval, on the other hand shows high polarization fraction with a very clear sinusoidal modulation in the azimuthal angle distribution in 200 — 300 keV (see Figure 16). The polarization angle is also constrained within 13° uncertainty. The Bayes factor for this interval in 200 — 300 keV is found to be ~ 2 with a false polarization detection probability by chance $< 1\%$ clearly signifying that the GRB is polarized at the later part of the emission at higher energies.

7. DISCUSSIONS AND CONCLUSIONS

We presented the spectral, timing and polarization analysis of GRB 171010A which has an observed flu-

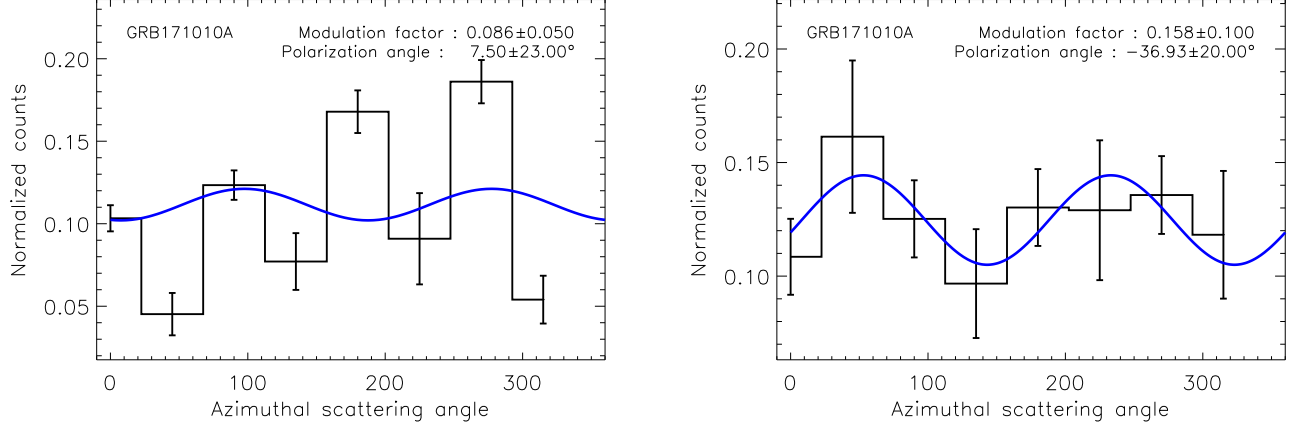


Figure 14. Same as Figure 12 but for different energy ranges — 100 — 200 keV (left) and 200 — 300 keV (right). We see a sinusoidal modulation in the 200 — 300 keV modulation curve.

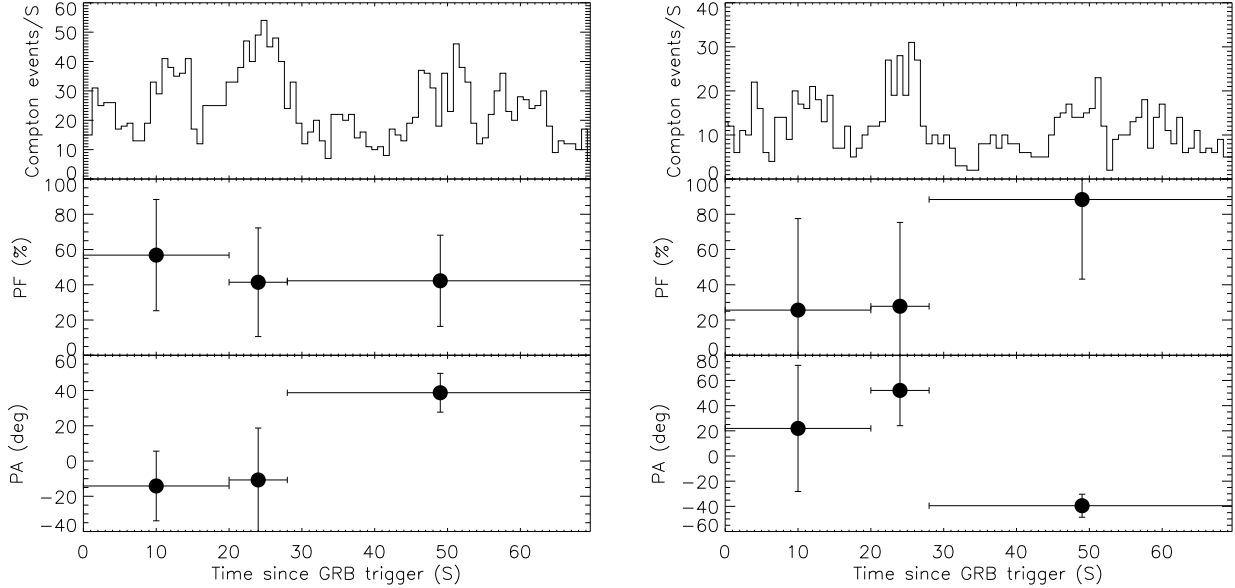


Figure 15. Compton light curve (top), polarization fraction (middle) and angle (bottom) for three different time intervals during the prompt emission of GRB 171010A in 100 — 200 keV (left) and 200 — 300 keV (right).

ence $> 10^{-4} \text{ ergs cm}^{-2}$. We found that the spectrum integrated over the duration of the burst is peculiar as it shows a low energy break and can be modeled by either a BB or another power law. Some GRBs have shown the presence of such a component which was modeled by a BB with peaks ranging up to 40 keV (Guiriec et al. 2011). **In a comprehensive joint analysis of X-rays and higher energies in the prompt emission, a break was found in the XRT-energy window (Zheng et al. 2012; Oganessian et al. 2018, 2017) and also in the GBM energy range (Ravasio et al.**

2018). To study the detailed evolution of the spectral parameters we sliced the spectrum into multiple time bins and found that Band E_p shows a bimodal distribution. Inclusion of a low energy component (modeled as a BB or a separate power-law) shows that the distribution of the peak energy remains > 100 keV and also falls in a concentrated region of between 100 — 200 keV. The mean value of the break energy in the power-law with two breaks model (E_2) is ~ 140 keV. The power law index above the break is softer than the index α obtained from the Band function. The mean value of

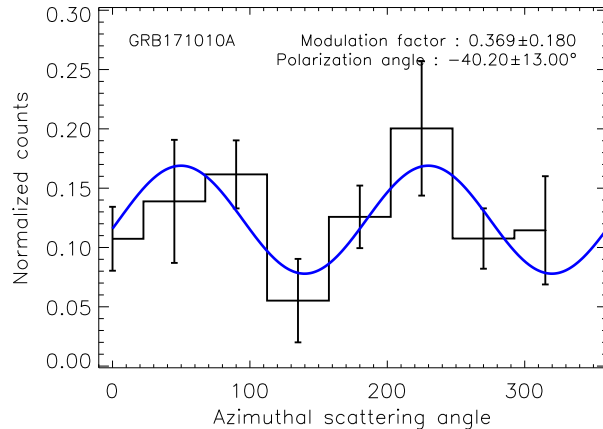


Figure 16. Azimuthal angle distribution for the third time interval (28 — 70 seconds at 200 — 300 keV). We see a clear and high modulation signature in the azimuthal distribution. The Bayes factor is found to be around 2 with a false polarization detection probability by chance less than 1 %.

$-\alpha_2$ is -1.45 and we are tempted to identify it with the synchrotron fast cooling process. E_2 can therefore be identified with the minimum energy injected to the electrons and the corresponding frequency is ν_m . On the other hand, $-\alpha_1$ is 0.3, harder than the value of spectral index $-2/3$ allowed below the cooling frequency ν_c of synchrotron radiation. However, absorption frequency which can be near the GBM lower energy window has expected index to be +1, thus it is possible that the cooling frequency falls very near to the absorption frequency. In such a case E_1 can be either identified as ν_c or ν_a as the ratio ν_c/ν_a or ν_a/ν_c will be closer to 1. Now, relating to the fast cooling scenario $-\alpha_3$ can be set equal to $-p/2 - 1$ to get the index of power-law distribution of electron energies. We get $p \simeq 3.2$ and for the distribution shown by $-\alpha_3$ allowed values of p fall in the range 2 to 4. The component at the low energy end can also be interpreted as being of photospheric origin, generated in a region that is optically thick to the radiation, and radiation escaping at a radius where it becomes transparent. **We have tested also the synchrotron model since bkn2pow gives a possibility that synchrotron model in marginally fast cooling regime could in principle work. The direct fitting of the prompt emission spectra by the synchrotron model have been performed in number of studies (Tavani 1996; Lloyd & Petrosian 2000; Burgess et al. 2014b; Zhang et al. 2016, 2018; Burgess et al. 2018) that give the preference to the slow or moderately fast cooling regimes of radiation. In our analysis, the synchrotron model returns small ratio between γ_m and γ_c , and the range of pstat/dof that is similar to other models and it has same number**

of parameters as Band function. Our results show that the spectral data can also be well described by a Comptonization (`grbcomp`) model.

From the afterglows observed in LAT (>100 MeV) and XRT (0.3 -10 keV), we concluded that the afterglows are produced in an external shock propagating into the ambient medium. By assuming the ambient medium to be homogeneous, we estimated the initial Lorentz factor of the ejecta. However, the Lorentz factor thus obtained is for the merged ejecta. The sub-MeV emission possibly arises from multiple internal shocks and a stratification in the Lorentz factor can not be ruled out. From the observed break in the XRT light curve, we obtained the jet opening angle. GRB 171010A consists of a jet with initial beaming angle much narrower than the jet opening angle.

The burst shows high polarization, however significant variation in the polarization fraction (PF) and angle (PA) can be seen with energy and time. Such variations in PA can arise due to ordered magnetic field or random magnetic fields produced in shocks and when within the beaming angle, the net magnetic field can be oriented in any direction independent of the other shells. For a high polarization, the coherence length of the magnetic field (θ_B) should be larger than or comparable to the beaming angle $1/\Gamma$ *i.e.* $\theta_B \gtrsim 1/\Gamma$. **In case of a Poynting flux dominated jet a pulse is produced in each ICMART event. The peak energy and polarisation decreases in each ICMART event. The polarisation degree and angle can vary (Zhang & Yan 2011; Deng et al. 2016). The spectrum can be a hybrid of blackbody and Band function. We have observed a low energy feature and the spectrum deviating from Band function**

which was also modelled by a blackbody. This can be contribution from a photosphere (Gao & Zhang 2015). The lower polarisation at energies below 200 keV can be due to multiple events superimposing and decreasing the net degree of polarization. The change in polarisation angle with energy also supports this argument. Therefore, the spectrum and polarization measurements are consistent with ICMART model.

In the Comptonization model multiple Compton scatterings are assumed, producing higher energy photons in the jet. The photons below the peak energy in the `grbcomp` model are produced by the Comptonization of the seed blackbody photons during the sub-relativistic phase. This component is, therefore, expected to be unpolarized. The high energy photons above the peak energy are mostly generated by further inverse Compton scattering off the non-thermal relativistic electrons of the relativistic outflow. This can give a polarization up to 100% when the emission is observed at an angle $1/\Gamma$ with the beaming axis and unpolarized when viewed on-axis (Rybicki & Lightman 1979). As for polarization, the highest value is expected for emission in the jet because in this case a photon, originating in the Compton cloud, illuminates the jet (or outflow) and undergoes a single up-scattering. Single scattering off jet electrons can result in a degree of polarization up to 100%. Change in the polarization fraction and angle can be possible only if jet is fragmented and we are observing it at different viewing angles. The measured high polarization below the peak is in contradiction with the predictions of this model.

The photospheric component found in the spectra suggests that the overall spectral shape may also be explained by the sub-photospheric dissipation model (Vurm & Beloborodov 2016). The polarization expected in the sub-photospheric dissipation model is low and tends to decrease at higher energies because the higher energy photons are produced deep within the photosphere and are reprocessed through multiple Compton scatterings before finally leaving the system at the photosphere (Lundman et al. 2016). The observed increase in the polarization with energy is in contradiction with the predictions of this model.

Another interpretation independent of the synchrotron or inverse Compton origin is that the emission is from fragmented fireballs moving with different velocity vectors (Lazzati & Begelman 2009). The fragments moving into the direction of the observer will have the least polarization. If the intrinsic brightness of all the fragments are the same then this would also be the brightest fragment. The fragments making larger

angle with the line of sight, on the other hand, will have higher polarization and lower intensity. The polarization angle can sweep randomly between different pulses in this setting. Another prediction of this geometry is that the PF and PA should not change within a single pulse. In time integrated analysis, we also find a change in polarization with energy. One possible explanation for this is that given the variability seen in the low energy light curve (100 - 200 keV), the contribution in this energy range could be from more fragments than that in the high energy light curve (200 - 300 keV). The averaging effect thus results in a relatively lower polarization fraction (maximum PF up to 100% can be achieved for the fragments viewed at $1/\Gamma$, where Γ is the Lorentz factor of a fragment) and a different position angle at lower energies in comparison to those in the high energy band. The change in polarization with time can be explained by temporally separated internal shocks produced in the different fragments. Therefore, the change in polarization from high to low seen in the 100 - 200 keV energy can be explained by considering the first pulse produced off-axis and the other brighter pulses near the axis (line of sight). In the high energy part, an increase in polarization with time is observed as well as the polarization angle are found to anti-correlate with the low energy counterpart. This suggests that the high energy emission has increased contribution with time from energetic off-axis fragments.

In the fragmented fireball scenario the jet should be fragmented into small scale ($\theta_{fragment} < \theta_{beam}$). The Lorentz factor Γ_0 was calculated from the LAT high energy afterglows that were produced in the external shocks. If the internal shocks were produced before the saturation in Lorentz factor was achieved then we can have a lower value of Lorentz factor when the internal shocks occur. This will allow a little room to increase θ_{beam} . If the internal shocks are produced at small radii, then the velocity vector within the θ_{beam} for a radially expanding ejecta will also have more divergence in their direction.

We conclude that the polarization results when used with spectral and temporal information are highly constraining. Although we cannot decisively select a single model, we find that models with a decrease in polarization with energy are either less probable or contributions from multiple underlying shocks in different energy ranges are needed to explain the apparent modulation with energy. Comptonization model has low polarization at low energies is contradiction with our observations. However independent of emission mechanisms, a geometric model consisting of multiple fragments can

explain the data, but demands fragmentation at small angular scale, well within θ_{beam} .

ACKNOWLEDGEMENTS

This research has made use of data obtained through the HEASARC Online Service, provided by the NASA-GSFC, in support of NASA High Energy Astrophysics Programs. This publication also uses the data from the AstroSat mission of the Indian Space Research Organisation (ISRO), archived at the Indian Space Science Data Centre (ISSDC). CZT-Imager is built by a con-

sortium of Institutes across India including Tata Institute of Fundamental Research, Mumbai, Vikram Sarabhai Space Centre, Thiruvananthapuram, ISRO Satellite Centre, Bengaluru, Inter University Centre for Astronomy and Astrophysics, Pune, Physical Research Laboratory, Ahmedabad, Space Application Centre, Ahmedabad: contributions from the vast technical team from all these institutes are gratefully acknowledged. The polarimetric computations were performed on the HPC resources at the Physical Research Laboratory (PRL). We thank Lev Titarchuk for discussions on the *grbcomp* model.

REFERENCES

- Abbott, B. P., Abbott, R., Abbott, T. D., et al. 2016, *Physical Review Letters*, 116, 061102
- Abdo, A. A., Ackermann, M., Ajello, M., et al. 2009, *ApJL*, 706, L138
- Ackermann, M., Asano, K., Atwood, W. B., et al. 2010, *ApJ*, 716, 1178
- Ackermann, M., Ajello, M., Asano, K., et al. 2013, *ApJS*, 209, 11
- Akerlof, C., Balsano, R., Barthelmy, S., et al. 1999, *Nature*, 398, 400
- Arnaud, K. A. 1996, in *Astronomical Society of the Pacific Conference Series*, Vol. 101, *Astronomical Data Analysis Software and Systems V*, ed. G. H. Jacoby & J. Barnes, 17
- Band, D., Matteson, J., Ford, L., et al. 1993, *ApJ*, 413, 281
- Basak, R., & Rao, A. R. 2015, *ApJ*, 812, 156
- Beloborodov, A. M. 2017, *ApJ*, 838, 125
- Beniamini, P., & Giannios, D. 2017, *MNRAS*, 468, 3202
- Burgess, J. M., Bégué, D., Bacelj, A., et al. 2018, *arXiv e-prints*, arXiv:1810.06965
- Burgess, J. M., Preece, R. D., Ryde, F., et al. 2014a, *ApJL*, 784, L43
- Burgess, J. M., Preece, R. D., Connaughton, V., et al. 2014b, *ApJ*, 784, 17
- Cano, Z., Wang, S.-Q., Dai, Z.-G., & Wu, X.-F. 2017, *Advances in Astronomy*, 2017, 8929054
- Chattopadhyay, T., Vadawale, S. V., Rao, A. R., Sreekumar, S., & Bhattacharya, D. 2014, *Experimental Astronomy*, 37, 555
- Chattopadhyay, T., Vadawale, S. V., Aarthy, E., et al. 2017, *ArXiv e-prints*, arXiv:1707.06595
- Covino, S., & Gotz, D. 2016, *Astronomical and Astrophysical Transactions*, 29, 205
- D’Ai, A., Melandri, A., Sbarufatti, B., et al. 2017, *GRB Coordinates Network*, Circular Service, No. 21989, #1-2018 (2017), 21989
- Dai, Z. G., & Lu, T. 1998, *A&A*, 333, L87
- Deng, W., Zhang, H., Zhang, B., & Li, H. 2016, *ApJL*, 821, L12
- Evans, P. A. 2017, *GRB Coordinates Network*, Circular Service, No. 21986, #1-2018 (2017), 21986
- Frail, D. A., Kulkarni, S. R., Sari, R., et al. 2001, *ApJL*, 562, L55
- Frederiks, D., Golenetskii, S., Aptekar, R., et al. 2017, *GRB Coordinates Network*, Circular Service, No. 22003, #1-2018 (2017), 22003
- Frontera, F., Amati, L., Farinelli, R., et al. 2013, *ApJ*, 779, 175
- Gao, H., & Zhang, B. 2015, *ApJ*, 801, 103
- Guiriec, S., Connaughton, V., Briggs, M. S., et al. 2011, *ApJL*, 727, L33
- Izzo, L., Ruffini, R., Penacchioni, A. V., et al. 2012, *A&A*, 543, A10
- Kankare, E., O’Neill, D., Izzo, L., et al. 2017, *GRB Coordinates Network*, Circular Service, No. 22002, #1-2018 (2017), 22002
- Komatsu, E., Dunkley, J., Nolta, M. R., et al. 2009, *ApJS*, 180, 330
- Lazzati, D., & Begelman, M. C. 2009, *ApJL*, 700, L141
- Lazzati, D., Ghisellini, G., Celotti, A., & Rees, M. J. 2000, *ApJL*, 529, L17
- Liang, E.-W., Yi, S.-X., Zhang, J., et al. 2010, *ApJ*, 725, 2209
- Lloyd, N. M., & Petrosian, V. 2000, *ApJ*, 543, 722
- Lundman, C., Vurm, I., & Beloborodov, A. M. 2016, *ArXiv e-prints*, arXiv:1611.01451
- Meszaros, P., & Rees, M. J. 1993, *ApJ*, 405, 278
- Mészáros, P., & Rees, M. J. 1997, *ApJ*, 476, 232

Table 2. LAT emission (> 100 MeV) in different time intervals for a fit with a power-law spectrum.

| Time (s) | Index | Energy flux ($10^{-9} \text{ ergs cm}^{-2} \text{ s}^{-1}$) | Photon flux ($\times 10^{-7} \text{ photons cm}^{-2} \text{ s}^{-1}$) | Test Statistic (TS) |
|-------------------|------------------|--|--|------------------------|
| (0) 0 - 346 | -2 (fixed) | < 14.4 | < 193 | 0 |
| (1) 346 - 514 | -2.35 ± 0.33 | 8.43 ± 3.33 | 170 ± 48 | 39 |
| (2) 514 - 635 | -1.97 ± 0.25 | 13.00 ± 5.25 | 167 ± 46 | 85 |
| (3) 635 - 1200 | -1.95 ± 0.25 | 3.46 ± 1.80 | 44 ± 13 | 62 |
| (4) 1200 - 2150 | -2.43 ± 0.36 | 1.23 ± 0.48 | 27 ± 8 | 33 |
| (5) 2150 - 6650 | -1.50 ± 0.23 | 1.43 ± 0.55 | 9.0 ± 1.4 | 58 |
| (6) 6650 - 100000 | -2 (fixed) | < 0.093 | < 2.2 | 9 |

Table 3. Best fit parameters for power law fits with multiple breaks for the low energy light curve from XRT. Power law with two breaks is the best fit model.

| breaks | α_1 | $t_{b,1}$ (10^4 s) | α_2 | $t_{b,2}$ (10^5 s) | α_3 | $t_{b,3}$ (10^5 s) | α_4 |
|--------|------------------------|--------------------------|-------------------------|--------------------------|------------------------|--------------------------|---------------|
| 1 | $1.30^{+0.07}_{-0.08}$ | $34.0^{+0.0}_{-15.0}$ | $2.0^{+0.0}_{-0.0}$ | | | | |
| 2 | $2.37^{+0.32}_{-0.17}$ | $8.6^{+1.6}_{-5.0}$ | $-0.95^{+2.13}_{-0.55}$ | $1.58^{+1.57}_{-0.14}$ | $1.85^{+0.14}_{-0.14}$ | | |
| 3 | $2.37^{+0.39}_{-0.16}$ | $7.0^{+0.0}_{+3.0}$ | 0^{+1}_{-2} | $1.8^{+0.0}_{-0.4}$ | $2.0^{+6.0}_{-0.5}$ | $8.0^{+0.0}_{-6.0}$ | 1^{+7}_{-3} |

Table 4. Spectral fit to the XRT spectra at different time intervals using the power law (PL) model

| Time (10^4 s) | Model | $n_{H,i}$ 10^{22} | α_{po} | CSTAT/dof |
|--------------------------|-------|------------------------|---------------------|-----------|
| Phase 1 (2.43 - 17.5) | PL | | $1.9^{+0.1}_{-0.1}$ | |
| Phase 2 (17.5, 132.2) | | $0.27^{+0.05}_{-0.05}$ | | 513/566 |
| Phase 1 (2.43, 2.58) | PL | | α_{po} | CSTAT/dof |
| (3.03, 3.17) | | $1.45^{+0.32}_{-0.70}$ | | 179/222 |
| (3.59, 4.16) | | $1.7^{+0.1}_{-0.1}$ | | 211/246 |
| (13.3, 17.5) | | $1.71^{+0.15}_{-0.15}$ | | 204/205 |
| Phase 2 (17.5, 77.2) | | $1.9^{+0.2}_{-0.2}$ | | 109/135 |
| (85, 132.2) | | $1.8^{+0.2}_{-0.2}$ | | 151/188 |
| | | $1.4^{+0.5}_{-0.4}$ | | 45/41 |

- , 1999, MNRAS, 306, L39
- Molinari, E., Vergani, S. D., Malesani, D., et al. 2007, A&A, 469, L13
- Narayan, R., Paczynski, B., & Piran, T. 1992, ApJL, 395, L83
- Nousek, J. A., Kouveliotou, C., Grupe, D., et al. 2006, ApJ, 642, 389
- Oganesyan, G., Nava, L., Ghirlanda, G., & Celotti, A. 2017, ApJ, 846, 137
- , 2018, A&A, 616, A138
- Omodei, N., Vianello, G., & Ahlgren, B. 2017, GRB Coordinates Network, Circular Service, No. 21985, #1-2018 (2017), 21985
- Page, K. L., Starling, R. L. C., Fitzpatrick, G., et al. 2011, MNRAS, 416, 2078
- Poolakkil, S., & Meegan, C. 2017, GRB Coordinates Network, Circular Service, No. 21992, #1-2018 (2017), 21992
- Ravasio, M. E., Oganesyan, G., Ghirlanda, G., et al. 2018, A&A, 613, A16
- Rees, M. J., & Meszaros, P. 1992, MNRAS, 258, 41P
- , 1994, ApJL, 430, L93
- Rybicki, G. B., & Lightman, A. P. 1979, Radiative processes in astrophysics
- Ryde, F. 2005, ApJL, 625, L95
- Sari, R., & Piran, T. 1999, ApJ, 520, 641

Table 5. Time-resolved Spectral fitting for different models

| Band | | α | β | E_p (keV) | K_B | pgstat/dof | | |
|------------------|--------------|---|---|--|---|-------------------------------------|---|------------|
| Sr. no. | (t_1, t_2) | | | | | | | |
| 1 | -1, 7 | -1.2 ^{+0.1} _{-0.1} | -9.3 ^{+19.4} _{-∞} | 141 ⁺¹⁶ ₋₁₉ | 0.016 ^{+0.004} _{-0.003} | 420/339 | | |
| 2 | 7, 9 | -1.10 ^{+0.05} _{-0.05} | -8.8 ^{+18.8} _{-∞} | 222 ⁺²⁸ ₋₂₃ | 0.029 ^{+0.004} _{-0.005} | 284/339 | | |
| 3 | 9, 10 | -1.08 ^{+0.1} _{-0.07} | -7.7 ^{+17.7} _{-∞} | 274 ⁺¹¹¹ ₋₇₄ | 0.054 ^{+0.011} _{-0.009} | 212/339 | | |
| 4 | 10, 12 | -1.0 ^{+0.1} _{-0.1} | -2.2 ^{+0.2} _{-0.5} | 303 ⁺¹⁰⁷ ₋₅₁ | 0.081 ^{+0.011} _{-0.011} | 310/339 | | |
| 5 | 12, 14 | -0.90 ^{+0.07} _{-0.06} | -2.3 ^{+0.2} _{-0.3} | 362 ⁺⁷² ₋₅₂ | 0.10 ^{+0.01} _{-0.01} | 311/339 | | |
| 6 | 14, 17 | -0.90 ^{+0.07} _{-0.06} | -2.15 ^{+0.10} _{-0.17} | 329 ⁺⁶³ ₋₅₀ | 0.09 ^{+0.01} _{-0.01} | 400/339 | | |
| 7 | 17, 18 | -0.8 ^{+0.1} _{-0.1} | -2.4 ^{+0.2} _{-0.4} | 206 ⁺⁴³ ₋₃₁ | 0.18 ^{+0.04} _{-0.03} | 290/339 | | |
| 8 | 18, 19 | -0.8 ^{+0.1} _{-0.1} | -2.40 ^{+0.17} _{-0.25} | 217 ⁺²⁷ ₋₂₃ | 0.23 ^{+0.03} _{-0.03} | 210/339 | | |
| 9 | 19, 20 | -0.82 ^{+0.07} _{-0.07} | -2.5 ^{+0.2} _{-0.3} | 241 ⁺³¹ ₋₂₇ | 0.26 ^{+0.03} _{-0.03} | 341/339 | | |
| 10 | 20, 24 | -0.80 ^{+0.03} _{-0.03} | -2.50 ^{+0.08} _{-0.01} | 230 ⁺¹¹ ₋₁₀ | 0.33 ^{+0.02} _{-0.01} | 620/339 | | |
| 11 | 24, 26 | -1.00 ^{+0.06} _{-0.06} | -2.6 ^{+0.2} _{-0.2} | 130 ⁺¹⁰ ₋₉ | 0.30 ^{+0.04} _{-0.30} | 443/339 | | |
| 12 | 26, 29 | -1.10 ^{+0.04} _{-0.03} | -2.8 ^{+0.2} _{-0.4} | 196 ⁺¹⁴ ₋₁₃ | 0.22 ^{+0.01} _{-0.01} | 519/339 | | |
| 13 | 29, 30 | -1.00 ^{+0.07} _{-0.06} | -2.8 ^{+0.3} _{-1.6} | 255 ⁺⁴⁰ ₋₃₀ | 0.22 ^{+0.03} _{-0.02} | 314/339 | | |
| 14 | 30, 31 | -1.00 ^{+0.04} _{-0.04} | -9.4 ^{+19.4} _{-∞} | 316 ⁺²⁸ ₋₂₆ | 0.24 ^{+0.02} _{-0.01} | 293/339 | | |
| 15 | 31, 32 | -0.83 ^{+0.05} _{-0.05} | -2.5 ^{+0.2} _{-0.3} | 284 ⁺³² ₋₂₆ | 0.35 ^{+0.03} _{-0.03} | 418/339 | | |
| 16 | 32, 34 | -0.82 ^{+0.03} _{-0.03} | -2.5 ^{+0.1} _{-0.1} | 273 ⁺¹⁷ ₋₁₅ | 0.43 ^{+0.02} _{-0.02} | 506/339 | | |
| 17 | 34, 35 | -0.80 ^{+0.05} _{-0.05} | -2.5 ^{+0.1} _{-0.2} | 264 ⁺²³ ₋₂₀ | 0.47 ^{+0.04} _{-0.03} | 314/339 | | |
| 18 | 35, 36 | -0.90 ^{+0.05} _{-0.05} | -2.7 ^{+0.2} _{-0.5} | 250 ⁺²⁴ ₋₂₁ | 0.40 ^{+0.03} _{-0.03} | 320/339 | | |
| 19 | 36, 38 | -0.80 ^{+0.04} _{-0.04} | -2.6 ^{+0.1} _{-0.1} | 134 ⁺⁷ ₋₆ | 0.49 ^{+0.04} _{-0.04} | 480/339 | | |
| 20 | 38, 39 | -1.0 ^{+0.1} _{-0.1} | -2.7 ^{+0.2} _{-0.4} | 101 ⁺¹⁰ ₋₉ | 0.35 ^{+0.07} _{-0.05} | 357/339 | | |
| 21 | 39, 41 | -0.3 ^{+0.3} _{-0.3} | -2.80 ^{+0.05} _{-0.06} | 42 ⁺⁵ ₋₄ | 2.59 ^{+3.07} _{-1.21} | 494/339 | | |
| 22 | 41, 44 | -1.25 ^{+0.04} _{-0.04} | -3 ^{+0.3} _{-0.7} | 110 ⁺⁷ ₋₆ | 0.23 ^{+0.02} _{-0.02} | 612/339 | | |
| 23 | 44, 45 | -1.1 ^{+0.1} _{-0.1} | -3 ^{+0.4} _{-∞} | 131 ⁺¹⁴ ₋₁₆ | 0.27 ^{+0.05} _{-0.04} | 288/339 | | |
| 24 | 45, 46 | -1.05 ^{+0.05} _{-0.05} | -2.8 ^{+0.3} _{-1.1} | 191 ⁺¹⁸ ₋₁₄ | 0.32 ^{+0.03} _{-0.03} | 366/339 | | |
| 25 | 46, 47 | -1.0 ^{+0.1} _{-0.1} | -2.5 ^{+0.2} _{-0.5} | 103 ⁺¹⁵ ₋₁₂ | 0.33 ^{+0.09} _{-0.06} | 356/339 | | |
| 26 | 47, 48 | -1.20 ^{+0.07} _{-0.07} | -9.4 ⁺¹⁹ _{-∞} | 98 ⁺⁷ ₋₆ | 0.21 ^{+0.03} _{-0.03} | 328/339 | | |
| 27 | 48, 50 | -1.2 ^{+0.2} _{-0.1} | -2.8 ^{+0.4} _{-1.2} | 65 ⁺⁷ ₋₁₀ | 0.17 ^{+0.10} _{-0.04} | 341/339 | | |
| 28 | 50, 51 | -1.1 ^{+0.1} _{-0.1} | -2.9 ^{+0.4} _{-1.1} | 93 ⁺¹¹ ₋₁₁ | 0.21 ^{+0.06} _{-0.04} | 291/339 | | |
| 29 | 51, 53 | -1.1 ^{+0.1} _{-0.1} | -2.8 ^{+0.2} _{-0.3} | 99 ⁺⁸ ₋₇ | 0.28 ^{+0.04} _{-0.03} | 397/339 | | |
| 30 | 53, 55 | -1.10 ^{+0.05} _{-0.04} | -3.3 ^{+0.6} _{-∞} | 208 ⁺¹⁷ ₋₁₉ | 0.21 ^{+0.02} _{-0.01} | 434/339 | | |
| 31 | 55, 56 | -1.00 ^{+0.05} _{-0.04} | -4.1 ^{+1.2} _{-∞} | 248 ⁺²² ₋₂₁ | 0.25 ^{+0.02} _{-0.02} | 329/339 | | |
| 32 | 56, 57 | -1.05 ^{+0.04} _{-0.04} | -9 ⁺¹⁹ _{-∞} | 268 ⁺²³ ₋₂₀ | 0.29 ^{+0.02} _{-0.02} | 339/339 | | |
| 33 | 57, 58 | -1.01 ^{+0.04} _{-0.04} | -9 ⁺¹⁹ _{-∞} | 252 ⁺¹⁹ ₋₁₈ | 0.36 ^{+0.02} _{-0.02} | 378/339 | | |
| 34 | 58, 59 | -1.00 ^{+0.05} _{-0.04} | -2.9 ^{+0.3} _{-1.0} | 245 ⁺²⁵ ₋₂₁ | 0.37 ^{+0.03} _{-0.01} | 390/339 | | |
| 35 | 59, 60 | -1.05 ^{+0.05} _{-0.05} | -2.9 ^{+0.3} _{-1.1} | 233 ⁺²⁶ ₋₂₃ | 0.31 ^{+0.03} _{-0.02} | 383/339 | | |
| 36 | 60, 61 | -1.00 ^{+0.06} _{-0.06} | -2.6 ^{+0.2} _{-0.6} | 212 ⁺²⁸ ₋₂₂ | 0.37 ^{+0.04} _{-0.03} | 369/339 | | |
| 37 | 61, 63 | -1.00 ^{+0.05} _{-0.05} | -2.5 ^{+0.2} _{-0.2} | 165 ⁺¹³ ₋₁₂ | 0.27 ^{+0.03} _{-0.02} | 421/339 | | |
| 38 | 63, 64 | -1.0 ^{+0.1} _{-0.1} | -2.7 ^{+0.3} _{-0.6} | 141 ⁺¹⁷ ₋₁₆ | 0.25 ^{+0.05} _{-0.04} | 305/339 | | |
| 39 | 64, 65 | -1.0 ^{+0.1} _{-0.1} | -2.8 ^{+0.3} _{-∞} | 154 ⁺²⁴ ₋₁₆ | 0.29 ^{+0.04} _{-0.04} | 316/339 | | |
| 40 | 65, 67 | -1.00 ^{+0.04} _{-0.04} | -2.8 ^{+0.2} _{-0.3} | 165 ⁺¹¹ ₋₁₀ | 0.39 ^{+0.03} _{-0.03} | 551/339 | | |
| 41 | 67, 68 | -1.04 ^{+0.06} _{-0.06} | -3 ^{+0.3} ₋₁ | 137 ⁺¹² ₋₁₁ | 0.39 ^{+0.05} _{-0.04} | 415/339 | | |
| 42 | 68, 69 | -1.03 ^{+0.05} _{-0.05} | -3 ^{+0.3} _{-0.7} | 153 ⁺¹² ₋₁₂ | 0.49 ^{+0.05} _{-0.04} | 382/339 | | |
| 43 | 69, 70 | -1.0 ^{+0.2} _{-0.1} | -2.30 ^{+0.13} _{-0.15} | 87 ⁺¹³ ₋₁₆ | 0.43 ^{+0.23} _{-0.09} | 389/339 | | |
| 44 | 70, 71 | -1.08 ^{+0.06} _{-0.06} | -2.80 ^{+0.25} _{-0.64} | 140 ⁺¹⁵ ₋₁₂ | 0.34 ^{+0.04} _{-0.04} | 379/339 | | |
| 45 | 71, 72 | -1.00 ^{+0.04} _{-0.02} | -9 ⁺¹⁹ _{-∞} | 158 ⁺⁸ ₋₄ | 0.46 ^{+0.03} _{-0.03} | 363/339 | | |
| 46 | 72, 73 | -1.02 ^{+0.09} _{-0.08} | -2.8 ^{+0.3} _{-0.4} | 93 ⁺⁸ ₋₈ | 0.39 ^{+0.08} _{-0.06} | 316/339 | | |
| 47 | 73, 74 | -0.9 ^{+0.8} _{-0.2} | -2.4 ^{+0.2} _{-0.2} | 56 ⁺¹² ₋₁₉ | 0.45 ^{+1.79} _{-0.18} | 315/339 | | |
| 48 | 74, 76 | -1.10 ^{+0.07} _{-0.06} | -2.8 ^{+0.2} _{-0.3} | 89 ⁺⁶ ₋₆ | 0.331 ^{+0.05} _{-0.04} | 506/339 | | |
| 49 | 76, 77 | -1.1 ^{+0.1} _{-0.1} | -2.9 ^{+0.4} _{-0.7} | 84 ⁺⁹ ₋₈ | 0.27 ^{+0.07} _{-0.05} | 313/339 | | |
| 50 | 77, 78 | -0.3 ^{+0.5} _{-0.9} | -2.1 ^{+0.1} _{-0.8} | 47 ⁺⁵⁷ ₋₈ | 1.68 ^{+3.71} _{-1.68} | 318/339 | | |
| 51 | 78, 82 | -1.2 ^{+0.1} _{-0.1} | -2.6 ^{+0.2} _{-0.2} | 75 ⁺⁷ ₋₇ | 0.15 ^{+0.03} _{-0.02} | 500/339 | | |
| 52 | 82, 84 | -1.1 ^{+0.1} _{-0.1} | -2.4 ^{+0.2} _{-0.2} | 139 ⁺¹⁵ ₋₁₄ | 0.20 ^{+0.03} _{-0.02} | 441/339 | | |
| 53 | 84, 85 | -1.1 ^{+0.2} _{-0.1} | -2.70 ^{+0.35} _{-∞} | 109 ⁺²⁸ ₋₁₇ | 0.11 ^{+0.04} _{-0.03} | 252/339 | | |
| 54 | 85, 90 | -1.2 ^{+0.2} _{-0.1} | -2.6 ^{+0.3} _{-0.1} | 76 ⁺⁷ ₋₁₄ | 0.13 ^{+0.08} _{-0.02} | 560/339 | | |
| 55 | 90, 101 | -1.2 ^{+0.1} _{-0.1} | -2.4 ^{+0.2} _{-0.3} | 83 ⁺⁹ ₋₁₀ | 0.06 ^{+0.02} _{-0.01} | 529/339 | | |
| 56 | 101, 113 | -1.30 ^{+0.08} _{-0.07} | -3.0 ^{+0.4} _{-1.0} | 86 ⁺⁸ ₋₈ | 0.04 ^{+0.01} _{-0.01} | 506/339 | | |
| 57 | 113, 136 | -1.3 ^{+0.1} _{-0.1} | -3 ^{+0.5} _{-0.8} | 66 ⁺⁴ ₋₆ | 0.036 ^{+0.008} _{-0.004} | 676/339 | | |
| 58 | 136, 137 | -1.3 ^{+0.1} _{-0.1} | -9 ⁺¹⁹ _{-∞} | 83 ⁺¹³ ₋₁₀ | 0.08 ^{+0.03} _{-0.02} | 266/339 | | |
| 59 | 137, 150 | -1.3 ^{+0.1} _{-0.1} | -3 ^{+0.4} _{-∞} | 66 ⁺⁵ ₋₅ | 0.04 ^{+0.01} _{-0.01} | 491/339 | | |
| 60 | 150, 171 | -1.1 ^{+1.4} _{-0.3} | -2.3 ^{+0.2} _{-0.2} | 33 ⁺⁸ ₋₁₂ | 0.04 ^{+0.26} _{-0.02} | 382/339 | | |
| Broken power-law | | | | | | | | |
| Sr. no. | (t_1, t_2) | α_1 | E_1 (keV) | α_2 | E_2 (keV) | β | K | pgstat/dof |
| 1 | -1, 7 | [-3.0] | 12.3 ^{+0.2} _{-1.1} | 1.6 ^{+0.6} _{-0.6} | 256 ⁺⁴⁷ ₋₁₂₂ | 7 ^{+∞} ₋₄ | 0.0001 ^{+0.0002} _{-0.00004} | 408/337 |
| 2 | 7, 9 | [-3.0] | 12.7 ^{+1.8} _{-2.0} | 1.4 ^{+0.1} _{-0.1} | 142 ⁺⁵⁹ ₋₂₈ | 2.4 ^{+0.6} _{-0.3} | 0.0002 ^{+0.0002} _{-0.00007} | 275/338 |
| 3 | 9, 10 | 0.9 ^{+0.7} _{-0.5} | 17 ^{+∞} ₋₁₇ | 1.3 ^{+0.1} _{-0.1} | 194 ⁺⁷³ ₋₅₁ | 2.5 ^{+0.7} _{-0.4} | 5 ⁺²⁹ ₋₅ | 215/338 |
| 4 | 10, 12 | -0.5 ^{+0.5} _{-∞} | 17.0 ^{+1.2} _{-1.5} | 1.25 ^{+0.05} _{-0.04} | 170 ⁺⁴¹ ₋₂₃ | 2.1 ^{+0.1} _{-0.1} | 0.14 ^{+0.02} _{-0.01} | 287/338 |
| 5 | 12, 14 | 0.2 ^{+0.6} _{-0.7} | 18 ⁺⁵ ₋₄ | 1.20 ^{+0.04} _{-0.05} | 212 ⁺⁵² ₋₂₇ | 2.2 ^{+0.1} _{-0.1} | 0.9 ^{+2.6} _{-0.9} | 315/337 |

Table 5. Time-resolved Spectral fitting (continued)

| Broken power-law | | | | | | | | | |
|------------------|----------------|--|---|--|---|--|---|------------|--|
| Sr. no. | (t_1, t_2) | α_1 | E_1 (keV) | α_2 | E_2 (keV) | β | K^b | pgstat/dof | |
| 6 | 14, 17 | -1 ⁺¹ ₋₁ | 16 ⁺³ ₋₂ | 1.20 ^{+0.05} _{-0.04} | 185 ⁺⁵⁰ ₋₂₂ | 2.1 ^{+0.1} _{-0.1} | 0.023 ^{+0.296} _{-0.023} | 373/337 | |
| 7 | 17, 18 | -0.8 ^{+0.8} _{-0.8} | 15 ⁺² ₋₂ | 1.10 ^{+0.07} _{-0.06} | 124 ⁺²³ ₋₁₃ | 2.2 ^{+0.1} _{-0.1} | 0.11 ^{+0.03} _{-0.02} | 288/338 | |
| 8 | 18, 19 | 0.4 ^{+0.3} _{-0.4} | 19 ^{+∞} ₋₁₉ | 1.00 ^{+0.06} _{-0.06} | 138.0 ^{+22.3} _{-15.4} | 2.2 ^{+0.1} _{-0.1} | 2.98 ^{+4.78} _{-2.98} | 218/338 | |
| 9 | 19, 20 | -0.2 ^{+0.8} _{-0.9} | 17 ⁺⁴ ₋₄ | 1.10 ^{+0.05} _{-0.05} | 146 ⁺¹⁵ ₋₁₂ | 2.3 ^{+0.1} _{-0.1} | 0.67 ^{+4.73} _{-0.67} | 337/337 | |
| 10 | 20, 24 | -0.2 ^{+0.4} _{-0.7} | 17 ⁺² ₋₂ | 1.10 ^{+0.02} _{-0.02} | 158 ⁺⁸ ₋₈ | 2.30 ^{+0.05} _{-0.05} | 0.80 ^{+1.43} _{-0.66} | 611/337 | |
| 11 | 24, 26 | -0.8 ^{+1.2} _{-0.8} | 15 ⁺⁵ ₋₂ | 1.40 ^{+0.06} _{-0.04} | 118 ⁺¹⁰ ₋₉ | 2.5 ^{+0.1} _{-0.1} | 0.25 ^{+2.07} _{-0.25} | 386/337 | |
| 12 | 26, 29 | 0.2 ^{+0.3} _{-0.5} | 18 ⁺² ₋₁ | 1.50 ^{+0.02} _{-0.02} | 352 ⁺²⁴ ₋₂₆ | 5.3 ^{+0.8} _{-0.6} | 0.013 ^{+0.001} _{-0.001} | 571/337 | |
| 13 | 29, 30 | -1.3 ^{+1.2} _{-0.8} | 15.5 ^{+2.5} _{-1.5} | 1.30 ^{+0.04} _{-0.04} | 205 ⁺³⁰ ₋₂₈ | 2.6 ^{+0.2} _{-0.2} | 0.044 ^{+0.490} _{-0.044} | 283/337 | |
| 14 | 30, 31 | -0.1 ^{+0.5} _{-0.6} | 15 ^{+∞} ₋₁₅ | 1.20 ^{+0.03} _{-0.03} | 177 ⁺¹⁵ ₋₁₄ | 2.4 ^{+0.1} _{-0.1} | 1.16 ^{+3.50} _{-2.16} | 298/338 | |
| 15 | 31, 32 | -0.6 ^{+0.4} _{-0.5} | 16.7 ^{+∞} _{-16.7} | 1.10 ^{+0.03} _{-0.03} | 186.0 ^{+20.4} _{-17.3} | 2.3 ^{+0.1} _{-0.1} | 0.35 ^{+0.70} _{-0.35} | 408/338 | |
| 16 | 32, 34 | -0.2 ^{+0.4} _{-0.8} | 18.0 ^{+2.7} _{-2.3} | 1.10 ^{+0.03} _{-0.03} | 175.0 ⁺¹¹ ₋₁₁ | 2.30 ^{+0.06} _{-0.05} | 1.09 ^{+2.17} _{-1.09} | 485/337 | |
| 17 | 34, 35 | 0.06 ^{+0.40} _{-0.60} | 19 ⁺⁴ ₋₄ | 1.10 ^{+0.04} _{-0.04} | 174 ⁺¹⁵ ₋₁₃ | 2.3 ^{+0.1} _{-0.1} | 2.15 ^{+4.08} _{-2.15} | 317/337 | |
| 18 | 35, 36 | 0.1 ^{+0.4} _{-0.7} | 18 ⁺³ ₋₃ | 1.10 ^{+0.04} _{-0.03} | 159 ⁺¹⁴ ₋₁₂ | 2.4 ^{+0.1} _{-0.1} | 2.31 ^{+4.52} _{-2.31} | 319/337 | |
| 19 | 36, 38 | -0.3 ^{+0.4} _{-0.6} | 17 ^{+1.4} _{-1.5} | 1.30 ^{+0.03} _{-0.03} | 116 ⁺⁷ ₋₆ | 2.50 ^{+0.07} _{-0.07} | 1.10 ^{+1.69} _{-1.10} | 386/337 | |
| 20 | 38, 39 | -0.3 ^{+0.5} _{-1.0} | 17 ⁺² ₋₂ | 1.60 ^{+0.05} _{-0.05} | 114 ⁺¹⁶ ₋₁₃ | 2.7 ^{+0.2} _{-0.2} | 0.94 ^{+2.66} _{-0.94} | 294/337 | |
| 21 | 39, 41 | 0.3 ^{+0.3} _{-0.3} | 19.0 ^{+1.5} _{-1.4} | 1.80 ^{+0.04} _{-0.05} | 126 ⁺²² ₋₂₂ | 3 ^{+0.3} _{-0.3} | 5.24 ^{+5.23} _{-3.10} | 391/337 | |
| 22 | 41, 44 | -0.6 ^{+0.2} _{-0.3} | 15 ^{+∞} ₋₁₅ | 1.60 ^{+0.02} _{-0.02} | 133 ⁺¹¹ ₋₁₀ | 2.80 ^{+0.14} _{-0.14} | 0.51 ^{+0.44} _{-0.29} | 443/338 | |
| 23 | 44, 45 | [-2.5] | 12.3 ^{+0.6} _{-0.7} | 1.40 ^{+0.04} _{-0.04} | 108 ⁺¹³ ₋₁₁ | 2.5 ^{+0.2} _{-0.1} | 0.005 ^{+0.001} _{-0.001} | 271/338 | |
| 24 | 45, 46 | [-2.0] | 14.4 ^{+0.6} _{-0.6} | 1.40 ^{+0.03} _{-0.03} | 169 ⁺¹⁶ ₋₂₁ | 2.6 ^{+0.2} _{-0.2} | 0.013 ^{+0.002} _{-0.001} | 292/338 | |
| 25 | 46, 47 | [-3.0] | 13.0 ^{+0.5} _{-0.5} | 1.50 ^{+0.04} _{-0.05} | 110 ⁺¹² ₋₁₇ | 2.5 ^{+0.2} _{-0.2} | 0.0012 ^{+0.0002} _{-0.0002} | 313/338 | |
| 26 | 47, 48 | [-3.0] | 13.0 ^{+0.6} _{-0.6} | 1.60 ^{+0.04} _{-0.05} | 121 ⁺¹⁷ ₋₁₇ | 3.0 ^{+0.3} _{-0.3} | 0.00128 ^{+0.0003} _{-0.0002} | 290/338 | |
| 27 | 48, 50 | [-3.0] | 12.6 ^{+0.4} _{-0.4} | 1.80 ^{+0.04} _{-0.05} | 104 ⁺¹³ ₋₂₃ | 3.0 ^{+0.4} _{-0.4} | 0.00114 ^{+0.0002} _{-0.0002} | 288/338 | |
| 28 | 50, 51 | [-3.0] | 13.3 ^{+0.7} _{-0.7} | 1.60 ^{+0.06} _{-0.06} | 109 ⁺²⁰ ₋₁₇ | 2.8 ^{+0.4} _{-0.3} | 0.00085 ^{+0.0002} _{-0.0002} | 255/338 | |
| 29 | 51, 53 | -0.8 ^{+0.8} _{-1.0} | 15.0 ^{+1.6} _{-1.4} | 1.60 ^{+0.04} _{-0.04} | 113 ⁺¹⁵ ₋₁₃ | 2.7 ^{+0.2} _{-0.2} | 0.24 ^{+1.53} _{-0.24} | 335/337 | |
| 30 | 53, 55 | [-3.0] | 13 ^{+0.4} _{-0.4} | 1.40 ^{+0.03} _{-0.03} | 157 ⁺¹⁷ ₋₁₄ | 2.5 ^{+0.1} _{-0.1} | 0.0011 ^{+0.0002} _{-0.0001} | 370/338 | |
| 31 | 55, 56 | -0.2 ^{+0.6} _{-0.7} | 17 ⁺³ ₋₃ | 1.30 ^{+0.04} _{-0.04} | 200 ⁺³¹ ₋₂₄ | 2.6 ^{+0.2} _{-0.2} | 0.88 ^{+3.29} _{-0.88} | 309/337 | |
| 32 | 56, 57 | -1.2 ^{+1.5} _{-0.9} | 14 ⁺⁴ ₋₁ | 1.30 ^{+0.04} _{-0.03} | 177 ⁺¹⁹ ₋₁₅ | 2.5 ^{+0.1} _{-0.1} | 0.09 ^{+0.96} _{-0.09} | 330/337 | |
| 33 | 57, 58 | -0.6 ⁺¹ _{-0.8} | 15.0 ^{+3.1} _{-2.3} | 1.30 ^{+0.03} _{-0.03} | 169 ⁺¹⁵ ₋₁₃ | 2.50 ^{+0.14} _{-0.12} | 0.56 ^{+2.12} _{-0.56} | 359/337 | |
| 34 | 58, 59 | -0.6 ^{+0.9} _{-0.5} | 15.0 ^{+3.0} _{-2.3} | 1.30 ^{+0.03} _{-0.03} | 168 ⁺¹⁴ ₋₁₂ | 2.4 ^{+0.1} _{-0.1} | 0.57 ^{+2.99} _{-0.57} | 366/337 | |
| 35 | 59, 60 | 0.4 ^{+0.3} _{-0.4} | 21.0 ^{+3.4} _{-2.8} | 1.40 ^{+0.04} _{-0.04} | 211 ⁺³⁶ ₋₂₅ | 2.6 ^{+0.2} _{-0.1} | 5.93 ^{+6.67} _{-4.02} | 364/337 | |
| 36 | 60, 61 | 0.2 ^{+0.4} _{-0.5} | 19.0 ^{+3.0} _{-2.3} | 1.40 ^{+0.04} _{-0.03} | 166 ⁺¹⁴ ₋₁₃ | 2.4 ^{+0.1} _{-0.1} | 3.40 ^{+5.85} _{-2.58} | 330/337 | |
| 37 | 61, 63 | [-3] | 13.0 ^{+0.5} _{-0.5} | 1.30 ^{+0.03} _{-0.03} | 120 ⁺⁹ ₋₉ | 2.3 ^{+0.1} _{-0.1} | 0.0012 ^{+0.0002} _{-0.0002} | 375/338 | |
| 38 | 63, 64 | -1.4 ^{+1.4} _{-∞} | 14 ⁺¹ ₋₁ | 1.30 ^{+0.05} _{-0.05} | 120 ⁺¹⁵ ₋₁₃ | 2.50 ^{+0.16} _{-0.15} | 0.04 ^{+0.007} _{-0.005} | 283/338 | |
| 39 | 64, 65 | 0.40 ^{+0.35} _{-0.40} | 21 ⁺³ ₋₃ | 1.50 ^{+0.06} _{-0.05} | 164 ⁺²³ ₋₂₆ | 2.7 ^{+0.2} _{-0.2} | 4.51 ^{+7.11} _{-3.04} | 289/337 | |
| 40 | 65, 67 | -0.8 ^{+0.7} _{-1.0} | 15.3 ^{+1.9} _{-1.6} | 1.00 ^{+0.03} _{-0.03} | 132 ⁺¹⁰ ₋₉ | 2.50 ^{+0.08} _{-0.08} | 0.32 ^{+1.68} _{-0.32} | 461/337 | |
| 41 | 67, 68 | -0.5 ^{+0.7} ₋₁ | 16.0 ^{+2.1} _{-1.6} | 1.40 ^{+0.04} _{-0.04} | 130 ⁺¹⁴ ₋₁₄ | 2.6 ^{+0.2} _{-0.2} | 0.81 ^{+3.82} _{-0.81} | 366/337 | |
| 42 | 68, 69 | 0.2 ^{+0.4} _{-0.6} | 18 ⁺³ ₋₄ | 1.4 ^{+0.05} _{-0.1} | 146 ⁺¹⁸ ₋₃₀ | 2.6 ^{+0.2} _{-0.3} | 5 ⁺¹⁰ ₋₅ | 340/337 | |
| 43 | 69, 70 | -0.07 ^{+0.4} _{-0.5} | 17.0 ^{+1.8} _{-1.7} | 1.60 ^{+0.05} _{-0.05} | 109 ⁺¹⁸ ₋₁₆ | 2.4 ^{+0.1} _{-0.1} | 2.15 ^{+4.62} _{-2.15} | 334/337 | |
| 44 | 70, 71 | 0.05 ^{+0.30} _{-0.50} | 18 ⁺² ₋₂ | 1.5 ^{+0.06} _{-0.04} | 154 ⁺²⁰ ₋₁₈ | 2.7 ^{+0.2} _{-0.2} | 2.62 ^{+3.64} _{-2.624} | 301/337 | |
| 45 | 71, 72 | -0.2 ^{+0.5} _{-0.5} | 17 ^{+1.8} _{-1.6} | 1.40 ^{+0.03} _{-0.03} | 149 ⁺¹² ₋₁₀ | 2.8 ^{+0.2} _{-0.1} | 1.59 ^{+3.97} _{-1.59} | 307/337 | |
| 46 | 72, 73 | 0.3 ^{+0.3} _{-0.5} | 18.2 ^{+2.2} _{-2.0} | 1.60 ^{+0.05} _{-0.05} | 105 ⁺¹⁰ ₋₉ | 2.70 ^{+0.14} _{-0.20} | 5.57 ^{+8.05} _{-5.57} | 275/337 | |
| 47 | 73, 74 | 0.4 ^{+0.3} _{-0.9} | 18 ⁺² ₋₅ | 1.8 ^{+0.1} _{-0.2} | 110 ⁺³¹ ₋₄₄ | 2.7 ^{+0.3} _{-0.4} | 5.60 ^{+8.12} _{-5.60} | 278/337 | |
| 48 | 74, 76 | -0.1 ^{+0.4} _{-0.8} | 16 ^{+1.5} _{-1.7} | 1.6 ^{+0.04} _{-0.05} | 108 ⁺¹² ₋₁₅ | 2.7 ^{+0.2} _{-0.2} | 1.86 ^{+3.62} _{-1.86} | 410/337 | |
| 49 | 76, 77 | 0.4 ^{+0.8} _{-0.5} | 19 ⁺³ ₋₂ | 1.70 ^{+0.06} _{-0.05} | 129 ⁺¹⁵ ₋₁₇ | 3.0 ^{+0.4} _{-0.3} | 4.52 ^{+8.12} _{-4.52} | 285/337 | |
| 50 | 77, 78 | -1 ⁺¹ ₋₁ | 15.0 ^{+3.3} _{-1.6} | 1.70 ^{+0.06} _{-0.06} | 136 ⁺²¹ ₋₃₄ | 3.0 ^{+0.4} _{-0.3} | 0.18 ^{+3.52} _{-0.18} | 271/337 | |
| 51 | 78, 82 | 0.3 ^{+0.3} _{-0.5} | 17.3 ^{+1.5} _{-1.7} | 1.80 ^{+0.04} _{-0.04} | 108 ⁺¹² ₋₁₀ | 2.7 ^{+0.2} _{-0.2} | 2.91 ^{+3.58} _{-2.15} | 381/337 | |
| 52 | 82, 84 | -1.3 ^{+0.9} _{-0.9} | 15.0 ^{+1.5} _{-1.1} | 1.50 ^{+0.04} _{-0.04} | 128 ⁺²⁰ ₋₁₅ | 2.4 ^{+0.2} _{-0.1} | 0.06 ^{+0.57} _{-0.06} | 352/337 | |
| 53 | 84, 85 | 0.3 ^{+0.6} _{-0.8} | 17.0 ^{+4.4} _{-5.3} | 1.6 ^{+0.1} _{-0.1} | 119 ⁺²³ ₋₂₄ | 2.6 ^{+0.4} _{-0.3} | 2.15 ^{+4.85} _{-2.15} | 238/337 | |
| 54 | 85, 90 | -0.2 ^{+0.6} _{-0.8} | 16 ⁺² ₋₂ | 1.80 ^{+0.04} _{-0.05} | 118 ⁺¹⁵ ₋₂₁ | 2.8 ^{+0.2} _{-0.2} | 0.71 ^{+2.27} _{-0.71} | 462/337 | |
| 55 | 90, 101 | [-2] | 12.7 ^{+0.4} _{-0.4} | 1.60 ^{+0.03} _{-0.05} | 101 ⁺¹³ ₋₂₃ | 2.5 ^{+0.2} _{-0.3} | 0.00456 ^{+0.00054} _{-0.00046} | 470/338 | |
| 56 | 101, 113 | [-3] | 12.8 ^{+0.4} _{-0.4} | 1.70 ^{+0.03} _{-0.03} | 122 ⁺¹⁴ ₋₁₂ | 2.9 ^{+0.3} _{-0.3} | 0.00027 ^{+0.00004} _{-0.00003} | 403/338 | |
| 57 | 113, 136 | [-3.0] | 12.20 ^{+0.04} _{-0.30} | 1.8 ^{+0.03} _{-0.06} | 97 ⁺¹⁵ ₋₁₅ | 2.9 ^{+0.4} _{-0.3} | 0.0003 ^{+0.000005} _{-0.00003} | 556/337 | |
| 58 | 136, 137 | [-3.0] | 12.4 ^{+0.9} _{-1.0} | 1.80 ^{+0.07} _{-0.06} | 181 ⁺⁵¹ ₋₆₈ | 5.1 ^{+∞} _{-2.2} | 0.0008 ^{+0.0003} _{-0.0002} | 256/338 | |
| 59 | 137, 150 | [-3.0] | 11.6 ^{+0.1} _{-0.4} | 1.70 ^{+0.04} _{-0.04} | 94 ⁺¹² ₋₁₀ | 2.9 ^{+0.4} _{-0.2} | 0.0004 ^{+0.0001} _{-0.00006} | 449/337 | |
| 60 | 150, 171 | 0.4 ^{+0.8} _{-0.8} | 14.0 ⁺⁴ _{-1.5} | 2.0 ^{+0.1} _{-0.1} | 95 ⁺³⁹ ₋₆₂ | 2.9 ^{+0.8} _{-0.6} | 0.93 ^{+5.78} _{-0.93} | 372/337 | |

b: photons keV⁻¹ cm⁻² s⁻¹ at 1 keV

Table 5. Time-resolved Spectral fitting (continued)

| BB+Band | (t ₁ , t ₂) | α | β | E_p (keV) | K_B | kT_{BB} (keV) | K_{BB} | pgstat/dof |
|---------|------------------------------------|---|---|--|---|--|---|------------|
| 1 | -1, 7 | -0.9 ^{+0.5} _{-0.3} | -9.4 ⁺¹⁹ _{-0.3} | 153 ⁺³⁴ ₋₂₃ | 0.02 ^{+0.01} _{-0.01} | 6.5 ^{+2.4} _{-1.6} | 0.50 ^{+0.39} _{-0.34} | 414/337 |
| 2 | 7, 9 | 0.01 ^{+1.80} _{-0.90} | -2.4 ^{+0.78} _{-0.3} | 149 ⁺⁶⁸ ₋₃₄ | 0.08 ^{+0.36} _{-0.05} | 5.5 ^{+1.3} _{-1.1} | 1.36 ^{+0.78} _{-0.81} | 276/337 |
| 3 | 9, 10 | -1.1 ^{+0.2} _{-0.2} | -9 ⁺¹⁹ _{-∞} | 299 ⁺¹⁹¹ ₋₄₁ | 0.05 ^{+0.01} _{-0.01} | 13 ^{+∞} ₋₈ | 0.73 ^{+2.00} _{-0.73} | 212/337 |
| 4 | 10, 12 | -0.4 ^{+0.4} _{-0.4} | -2.1 ^{+0.1} _{-0.2} | 215 ⁺⁸¹ ₋₃₄ | 0.12 ^{+0.06} _{-0.04} | 7.0 ^{+1.5} _{-1.0} | 2.55 ^{+0.78} _{-1.03} | 296/337 |
| 5 | 12, 14 | -0.8 ^{+0.2} _{-0.3} | -2.2 ^{+0.1} _{-0.3} | 331 ⁺³⁸³ ₋₅₉ | 0.10 ^{+0.02} _{-0.04} | 7.2 ^{+∞} _{-3.1} | 0.79 ^{+1.05} _{-0.79} | 309/337 |
| 6 | 14, 17 | -0.5 ^{+0.4} _{-0.2} | -2.1 ^{+0.1} _{-0.1} | 260 ⁺⁶⁶ ₋₅₄ | 0.11 ^{+0.03} _{-0.02} | 8.0 ^{+1.5} _{-1.1} | 2.09 ^{+0.90} _{-0.88} | 383/337 |
| 7 | 17, 18 | -0.5 ^{+0.5} _{-0.2} | -2.3 ^{+0.2} _{-0.3} | 185 ⁺⁵¹ ₋₃₄ | 0.22 ^{+0.17} _{-0.04} | 7 ⁺⁷ ₋₂ | 2.13 ^{+2.20} _{-1.90} | 287/337 |
| 8 | 18, 19 | -0.7 ^{+0.3} _{-0.4} | -2.4 ^{+0.2} _{-0.3} | 219 ⁺²¹⁹ ₋₃₄ | 0.23 ^{+0.08} _{-0.12} | 10 ^{+∞} ₋₁₀ | 1.20 ^{+2.24} _{-2.0} | 209/337 |
| 9 | 19, 20 | -0.6 ^{+0.5} _{-0.2} | -2.4 ^{+0.2} _{-0.3} | 218 ⁺⁴² ₋₄₁ | 0.31 ^{+0.17} _{-0.06} | 7.0 ^{+3.0} _{-1.5} | 3.16 ^{+2.99} _{-2.21} | 335/337 |
| 10 | 20, 24 | -0.5 ^{+0.1} _{-0.1} | -2.4 ^{+0.1} _{-0.1} | 212 ⁺¹⁴ ₋₁₂ | 0.39 ^{+0.04} _{-0.04} | 7.3 ^{+0.8} _{-0.6} | 4.26 ^{+1.19} _{-1.14} | 579/337 |
| 11 | 24, 26 | -0.1 ^{+0.4} _{-0.3} | -2.5 ^{+0.1} _{-0.1} | 122 ⁺¹⁰ ₋₉ | 0.63 ^{+0.41} _{-0.19} | 6.0 ^{+0.4} _{-0.4} | 7.79 ^{+2.14} _{-1.94} | 390/337 |
| 12 | 26, 29 | -0.8 ^{+0.1} _{-0.1} | -10.0 ^{+0.0} _{-∞} | 196 ⁺⁸ ₋₇ | 0.25 ^{+0.02} _{-0.02} | 6.0 ^{+0.5} _{-0.5} | 4.55 ^{+0.99} _{-0.94} | 458/337 |
| 13 | 29, 30 | -0.5 ^{+0.1} _{-0.2} | -2.6 ^{+0.2} _{-0.3} | 213 ⁺³³ ₋₂₁ | 0.30 ^{+0.11} _{-0.06} | 7.0 ^{+0.9} _{-0.8} | 5.63 ^{+2.14} _{-2.08} | 293/337 |
| 14 | 30, 31 | -0.7 ^{+0.2} _{-0.2} | -3.0 ^{+0.2} _{-0.6} | 256 ⁺⁵⁹ ₋₃₁ | 0.29 ^{+0.06} _{-0.04} | 5.7 ^{+1.5} _{-1.2} | 2.74 ^{+2.03} _{-1.37} | 289/337 |
| 15 | 31, 32 | -0.6 ^{+0.2} _{-0.2} | -2.4 ^{+0.1} _{-0.2} | 254 ⁺³⁸ ₋₂₆ | 0.40 ^{+0.08} _{-0.06} | 7.4 ^{+2.3} _{-1.5} | 4.14 ^{+2.57} _{-2.36} | 409/337 |
| 16 | 32, 34 | -0.5 ^{+0.1} _{-0.1} | -2.4 ^{+0.1} _{-0.1} | 241 ⁺²⁰ ₋₁₈ | 0.52 ^{+0.07} _{-0.05} | 8.0 ^{+0.7} _{-0.6} | 7.67 ^{+2.13} _{-2.00} | 460/337 |
| 17 | 34, 35 | -0.5 ^{+0.2} _{-0.1} | -2.4 ^{+0.1} _{-0.1} | 241 ⁺²⁷ ₋₂₆ | 0.54 ^{+0.11} _{-0.07} | 7.7 ^{+1.6} _{-1.2} | 5.62 ^{+3.14} _{-2.78} | 302/337 |
| 18 | 35, 36 | -0.6 ^{+0.3} _{-0.2} | -2.6 ^{+0.2} _{-0.3} | 224 ⁺³² ₋₃₀ | 0.46 ^{+0.13} _{-0.07} | 6.7 ^{+1.9} _{-1.2} | 4.25 ^{+3.03} _{-2.56} | 313/337 |
| 19 | 36, 38 | 0.1 ^{+0.4} _{-0.3} | -2.5 ^{+0.1} _{-0.1} | 122 ⁺⁸ ₋₇ | 1.23 ^{+0.70} _{-0.36} | 6.0 ^{+0.3} _{-0.3} | 11.35 ^{+2.50} _{-2.35} | 400/337 |
| 20 | 38, 39 | 0.3 ⁺¹ _{-0.6} | -2.7 ^{+0.2} _{-0.2} | 103.0 ^{+10.5} _{-9.5} | 1.21 ^{+3.03} _{-0.61} | 5.9 ^{+0.4} _{-0.4} | 11.89 ^{+3.33} _{-3.15} | 305/337 |
| 21 | 39, 41 | -0.4 ^{+0.5} _{-0.3} | -2.8 ^{+0.2} _{-0.3} | 99 ⁺⁸ ₋₉ | 0.50 ^{+0.45} _{-0.16} | 6.0 ^{+0.4} _{-0.3} | 11.20 ^{+2.22} _{-1.93} | 399/337 |
| 22 | 41, 44 | -0.4 ^{+0.3} _{-0.2} | -2.8 ^{+0.2} _{-0.2} | 116 ⁺⁷ ₋₇ | 0.49 ^{+0.20} _{-0.11} | 5.5 ^{+0.2} _{-0.2} | 10.36 ^{+1.60} _{-1.48} | 456/337 |
| 23 | 44, 45 | -0.5 ^{+0.5} _{-0.4} | -2.6 ^{+0.2} _{-0.3} | 116 ⁺¹⁷ ₋₁₂ | 0.52 ^{+0.49} _{-0.19} | 5.0 ^{+0.8} _{-0.6} | 6.01 ^{+5.02} _{-2.89} | 276/337 |
| 24 | 45, 46 | -0.4 ^{+0.2} _{-0.1} | -2.5 ^{+0.1} _{-0.2} | 167 ⁺¹⁶ ₋₉ | 0.53 ^{+0.06} _{-0.10} | 6.5 ^{+0.4} _{-0.5} | 10.77 ^{+1.56} _{-1.48} | 317/337 |
| 25 | 46, 47 | -0.2 ^{+0.8} _{-0.5} | -2.5 ^{+0.2} _{-0.3} | 107 ⁺¹⁶ ₋₁₃ | 0.70 ^{+1.17} _{-0.5} | 6.0 ^{+0.7} _{-0.5} | 9.29 ^{+3.36} _{-2.90} | 320/337 |
| 26 | 47, 48 | -0.3 ^{+0.7} _{-0.5} | -3.1 ^{+0.4} _{-∞} | 108 ⁺¹⁴ ₋₁₀ | 0.45 ^{+0.51} _{-0.19} | 5.7 ^{+0.6} _{-0.5} | 8.26 ^{+2.63} _{-2.73} | 293/337 |
| 27 | 48, 50 | -0.3 ^{+1.1} _{-0.5} | -2.8 ^{+0.3} _{-0.6} | 81 ⁺⁸ ₋₆ | 0.42 ^{+1.75} _{-0.21} | 4.95 ^{+0.40} _{-0.34} | 5.87 ^{+2.05} _{-1.80} | 303/337 |
| 28 | 50, 51 | 0.1 ^{+1.3} _{-0.7} | -2.8 ^{+0.3} _{-0.6} | 99 ⁺¹² ₋₁₂ | 0.67 ^{+2.82} _{-0.38} | 5.5 ^{+0.5} _{-0.5} | 6.90 ^{+2.59} _{-2.59} | 268/337 |
| 29 | 51, 53 | -0.4 ^{+0.3} _{-0.3} | -2.7 ^{+0.2} _{-0.2} | 100 ⁺⁸ ₋₇ | 0.58 ^{+0.29} _{-0.17} | 5.0 ^{+∞} _{-0.1} | 6.53 ^{+1.43} _{-1.77} | 354/337 |
| 30 | 53, 55 | -0.7 ^{+0.2} _{-0.2} | -2.7 ^{+0.2} _{-0.4} | 177 ⁺²¹ ₋₁₇ | 0.29 ^{+0.07} _{-0.05} | 6.0 ^{+0.6} _{-0.5} | 5.09 ^{+1.56} _{-1.55} | 402/337 |
| 31 | 55, 56 | -0.7 ^{+0.2} _{-0.1} | -4 ⁺¹ _{-∞} | 241 ⁺²³ ₋₂₆ | 0.28 ^{+0.05} _{-0.03} | 7 ⁺¹ ₋₁ | 5.48 ^{+2.13} _{-1.98} | 307/337 |
| 32 | 56, 57 | -0.9 ^{+0.1} _{-0.1} | -9 ⁺¹⁹ _{-∞} | 267 ⁺²³ ₋₂₀ | 0.305 ^{+0.065} _{-0.022} | 7.5 ^{+1.4} _{-1.2} | 4.87 ^{+2.21} _{-2.12} | 325/337 |
| 33 | 57, 58 | -0.8 ^{+0.1} _{-0.1} | -3.1 ^{+0.5} _{-∞} | 234 ⁺²⁵ ₋₂₅ | 0.41 ^{+0.07} _{-0.05} | 7 ⁺¹ ₋₁ | 6.84 ^{+2.57} _{-2.49} | 356/337 |
| 34 | 58, 59 | -0.7 ^{+0.2} _{-0.2} | -2.6 ^{+0.2} _{-0.4} | 219 ⁺²⁹ ₋₂₃ | 0.44 ^{+0.09} _{-0.06} | 7 ⁺¹ ₋₁ | 7.37 ^{+2.83} _{-2.67} | 367/337 |
| 35 | 59, 60 | -0.8 ^{+0.2} _{-0.1} | -2.8 ^{+0.3} _{-0.6} | 225 ⁺³¹ ₋₂₆ | 0.34 ^{+0.06} _{-0.04} | 8 ⁺¹ ₋₁ | 6.39 ^{+2.38} _{-2.4} | 359/337 |
| 36 | 60, 61 | -0.6 ^{+0.3} _{-0.2} | -2.5 ^{+0.14} _{-0.3} | 190 ⁺³⁵ ₋₂₀ | 0.48 ^{+0.14} _{-0.10} | 7.0 ^{+1.0} _{-0.7} | 9.53 ^{+3.05} _{-2.75} | 330/337 |
| 37 | 61, 63 | -0.5 ^{+0.4} _{-0.3} | -2.40 ^{+0.12} _{-0.15} | 143 ⁺¹⁷ ₋₁₅ | 0.46 ^{+0.24} _{-0.12} | 5.7 ^{+0.5} _{-0.4} | 5.83 ^{+2.04} _{-1.88} | 389/337 |
| 38 | 63, 64 | -0.4 ^{+0.3} _{-0.4} | -2.5 ^{+0.2} _{-0.2} | 130 ⁺¹⁸ ₋₁₈ | 0.41 ^{+0.40} _{-0.14} | 6.0 ^{+0.8} _{-0.8} | 4.68 ^{+2.49} _{-2.28} | 293/337 |
| 39 | 64, 65 | -0.80 ^{+0.40} _{-0.15} | -3.4 ^{+0.8} _{-3.4} | 182 ⁺²⁵ ₋₃₄ | 0.28 ^{+0.15} _{-0.05} | 8.4 ^{+1.4} _{-1.5} | 7.31 ^{+2.35} _{-2.24} | 285/337 |
| 40 | 65, 67 | -0.3 ^{+0.2} _{-0.2} | -2.6 ^{+0.1} _{-0.1} | 146 ⁺¹⁰ ₋₉ | 0.69 ^{+0.19} _{-0.13} | 6.3 ^{+0.3} _{-0.2} | 10.53 ^{+2.00} _{-1.98} | 464/337 |
| 41 | 67, 68 | -0.4 ^{+0.4} _{-0.3} | -2.7 ^{+0.2} _{-0.3} | 132 ⁺¹³ ₋₁₁ | 0.66 ^{+0.34} _{-0.17} | 6.0 ^{+0.6} _{-0.5} | 10.57 ^{+3.19} _{-2.93} | 373/337 |
| 42 | 68, 69 | -0.6 ^{+0.3} _{-0.2} | -2.7 ^{+0.2} _{-0.4} | 147 ⁺¹⁵ ₋₁₃ | 0.69 ^{+0.24} _{-0.14} | 6.4 ^{+0.7} _{-0.5} | 11.30 ^{+3.22} _{-3.00} | 336/337 |
| 43 | 69, 70 | -0.15 ^{+1.1} _{-0.5} | -2.4 ^{+0.1} _{-0.2} | 97 ⁺¹⁸ ₋₁₅ | 0.96 ^{+2.77} _{-0.51} | 6.0 ^{+0.7} _{-0.4} | 11.53 ^{+4.10} _{-3.46} | 345/337 |
| 44 | 70, 71 | -0.5 ^{+0.3} _{-0.2} | -2.7 ^{+0.2} _{-0.3} | 141 ⁺¹⁴ ₋₁₃ | 0.53 ^{+0.23} _{-0.12} | 6.0 ^{+0.5} _{-0.5} | 11.14 ^{+2.70} _{-2.53} | 318/337 |
| 45 | 71, 72 | -0.5 ^{+0.2} _{-0.2} | -3.2 ^{+0.3} _{-1.0} | 153 ⁺¹⁰ ₋₁₀ | 0.65 ^{+0.17} _{-0.11} | 6.0 ^{+0.6} _{-0.5} | 10.67 ^{+2.90} _{-2.84} | 317/337 |
| 46 | 72, 73 | 0.1 ^{+1.1} _{-0.6} | -2.7 ^{+0.2} _{-0.3} | 97 ⁺¹⁰ ₋₈ | 1.25 ^{+3.44} _{-0.67} | 6.0 ^{+0.4} _{-0.4} | 11.90 ^{+4.22} _{-3.81} | 276/337 |
| 47 | 73, 74 | 0.1 ^{+∞} _{-0.6} | -2.6 ^{+0.2} _{-0.2} | 81 ⁺¹⁰ ₋₉ | 1.04 ^{+0.29} _{-0.03} | 5.2 ^{+0.4} _{-0.3} | 9.73 ^{+1.28} _{-0.47} | 275/337 |
| 48 | 74, 76 | 0.1 ^{+0.8} _{-0.4} | -2.7 ^{+0.2} _{-0.2} | 95 ⁺⁷ ₋₈ | 1.14 ^{+2.26} _{-0.49} | 5.5 ^{+0.3} _{-0.3} | 11.56 ^{+2.80} _{-2.38} | 413/337 |
| 49 | 76, 77 | -0.5 ^{+0.5} _{-0.4} | -3 ^{+0.3} _{-0.7} | 98 ⁺¹¹ ₋₉ | 0.40 ^{+0.36} _{-0.15} | 6.0 ^{+0.9} _{-0.6} | 6.66 ^{+2.54} _{-2.30} | 290/337 |
| 50 | 77, 78 | -0.5 ^{+0.6} _{-0.4} | -2.8 ^{+0.3} _{-0.6} | 111 ⁺¹⁵ ₋₁₃ | 0.38 ^{+0.42} _{-0.14} | 6.2 ^{+0.7} _{-0.5} | 9.02 ^{+2.62} _{-2.52} | 275/337 |
| 51 | 78, 82 | 0.0 ^{+0.7} _{-0.4} | -2.7 ^{+0.2} _{-0.2} | 91 ⁺⁶ ₋₆ | 0.49 ^{+0.66} _{-0.21} | 5.0 ^{+0.2} _{-0.2} | 6.57 ^{+1.23} _{-1.20} | 386/337 |
| 52 | 82, 84 | -0.3 ^{+0.5} _{-0.3} | -2 ^{+0.1} _{-0.2} | 131 ⁺¹⁵ ₋₁₅ | 0.38 ^{+0.28} _{-0.11} | 6.0 ^{+0.5} _{-0.4} | 6.61 ^{+1.67} _{-1.55} | 380/337 |
| 53 | 84, 85 | 0.4 ^{+4.0} _{-1.0} | -2.6 ^{+0.3} _{-0.4} | 104 ⁺¹⁷ ₋₁₉ | 0.54 ^{+60.34} _{-0.36} | 5.5 ^{+0.8} _{-0.6} | 5.13 ^{+2.04} _{-2.06} | 235/337 |
| 54 | 85, 90 | -0.3 ⁺¹ _{-0.4} | -2.6 ^{+0.2} _{-0.2} | 91 ⁺⁸ ₋₁₁ | 0.31 ^{+0.43} _{-0.12} | 5.3 ^{+0.3} _{-0.3} | 4.64 ^{+1.39} _{-0.97} | 463/337 |
| 55 | 90, 101 | -0.2 ^{+4.5} _{-0.4} | -2.5 ^{+0.2} _{-0.2} | 88 ^{+101.02} ₋₂₀ | 0.17 ^{+75.02} _{-0.08} | 5 ^{+0.3} _{-0.3} | 2.02 ^{+1.19} _{-0.53} | 477/337 |
| 56 | 101, 113 | -0.3 ^{+0.5} _{-0.4} | -3 ^{+0.3} _{-0.5} | 100 ⁺¹⁰ ₋₈ | 0.09 ^{+0.08} _{-0.03} | 5 ^{+0.3} _{-0.3} | 1.69 ^{+0.36} _{-0.36} | 441/337 |
| 57 | 113, 136 | 0.25 ^{+0.25} _{-0.90} | -2.6 ^{+0.2} _{-0.6} | 72 ⁺¹¹ ₋₁₁ | 0.27 ^{+40.62} _{-0.19} | 4.5 ^{+0.2} _{-0.2} | 1.65 ^{+0.56} _{-0.46} | 610/337 |
| 58 | 136, 137 | -0.8 ^{+0.6} _{-0.4} | -9.3 ^{+3.3} ₋₁₅ | 103 ⁺¹⁸ ₋₁₅ | 0.11 ^{+0.102} _{-0.04} | 5.0 ^{+0.8} _{-0.7} | 2.85 ^{+1.71} _{-1.70} | 257/337 |
| 59 | 137, 150 | -0.5 ^{+0.7} _{-0.4} | -3 ^{+0.3} _{-0.6} | 79 ⁺⁶ ₋₆ | 0.10 ^{+0.15} _{-0.04} | 4.0 ^{+0.3} _{-0.3} | 1.40 ^{+0.49} _{-0.47} | 463/337 |
| 60 | 150, 171 | -1.1 ^{+1.1} _{-0.4} | -2.8 ^{+0.5} _{-∞} | 63 ⁺¹⁶ ₋₂₄ | 0.02 ^{+0.36} _{-0.01} | 4 ⁺¹ ₋₁ | 0.57 ^{+0.84} _{-0.30} | 374/337 |

Table 5. Time-resolved Spectral fitting (continued)

| grbcomp | | | | | | | | | |
|---------|-----------------------------------|-------------------------------------|--|--------------------------------------|--------------|---------------------------------------|--|------------|--|
| Sr. no. | (t ₁ ,t ₂) | kT _s (keV) | kT _e (keV) | τ | δ | α _b | R _{ph} (10 ¹⁰) cm | pgstat/dof | |
| 1 | -1, 7 | [5.3] | 90 ⁺⁴ ₋₁₄ | [3.2] | 1.50 ± -0.05 | 30 ^{+∞} ₋₂₄ | 8.7 ^{+0.2} _{-0.3} | 412/339 | |
| 2 | 7, 9 | [4.1] | 77 ⁺²⁰ ₋₃₂ | 4.0 ^{+1.5} _{-0.9} | 1.80 ± 0.07 | 2.6 ^{+∞} _{-1.3} | 17 ⁺¹ ₋₁ | 281/338 | |
| 3 | 9, 10 | [4.5] | 78 ⁺⁴⁰ ₋₃₂ | 4 ⁺¹ ₋₁ | 1.70 ± 0.06 | 1.8 ^{+1.6} _{-0.7} | 20 ⁺¹ ₋₁ | 213/338 | |
| 4 | 10, 12 | 7.7 ^{+1.5} _{-1.8} | 117 ⁺⁹⁰ ₋₆₂ | 3.0 ^{+2.1} _{-0.8} | 1.20 ± 0.03 | 1.4 ^{+0.6} _{-0.3} | 10 ⁺⁶ ₋₂ | 287/337 | |
| 5 | 12, 14 | 6.5 ^{+1.7} _{-2.6} | 86 ⁺³⁰ ₋₂₂ | 4 ⁺¹ ₋₁ | 1.60 ± 0.05 | 1.3 ^{+0.2} _{-0.2} | 14 ⁺¹⁷ ₋₄ | 305/337 | |
| 6 | 14, 17 | 8.1 ^{+1.5} _{-1.7} | 91 ⁺⁴⁵ ₋₃₁ | 3.6 ^{+1.5} _{-0.8} | 1.50 ± 0.05 | 1.2 ^{+0.2} _{-0.1} | 9 ⁺⁴ ₋₂ | 371/337 | |
| 7 | 17, 18 | [7] | 57 ⁺³² ₋₁₈ | 5.0 ^{+2.7} _{-1.4} | 2.40 ± 0.13 | 1.4 ^{+0.4} _{-0.2} | 14.7 ^{+0.3} _{-0.3} | 283/338 | |
| 8 | 18, 19 | [6] | 58 ⁺¹⁶ ₋₁₂ | 5 ⁺¹ ₋₁ | 2.36 ± 0.12 | 1.4 ^{+0.3} _{-0.2} | 21.6 ^{+0.4} _{-0.4} | 207/338 | |
| 9 | 19, 20 | 7.4 ^{+1.7} _{-2.3} | 62 ⁺¹⁹ ₋₁₆ | 4.5 ^{+2.0} _{-1.0} | 2.20 ± 0.10 | 1.5 ^{+0.3} _{-0.2} | 17 ⁺¹⁶ ₋₄ | 329/337 | |
| 10 | 20, 24 | 7.3 ^{+0.7} _{-0.8} | 63 ⁺⁷ ₋₆ | 4.8 ^{+0.5} _{-0.4} | 2.2 ± 0.1 | 1.5 ^{+0.1} _{-0.1} | 19 ⁺⁴ ₋₂ | 551/337 | |
| 11 | 24, 26 | 7.6 ^{+0.7} _{-0.7} | 35.5 ^{+11.5} _{-9.3} | 7 ⁺¹⁵ ₋₂ | 3.8 ± 0.3 | 1.6 ^{+0.3} _{-0.2} | 17 ⁺³ ₋₂ | 386/337 | |
| 12 | 26, 29 | 6.8 ^{+0.5} _{-0.5} | 53.0 ^{+9.8} _{-7.8} | 5.0 ^{+1.0} _{-0.7} | 2.6 ± 0.14 | 1.70 ^{+0.2} _{-0.15} | 20 ⁺³ ₋₂ | 462/337 | |
| 13 | 29, 30 | 7.7 ^{+1.1} _{-1.2} | 69 ⁺²² ₋₁₇ | 4.5 ^{+1.5} _{-0.9} | 2.0 ± 0.1 | 1.7 ^{+0.4} _{-0.2} | 16 ⁺³ ₋₃ | 286/337 | |
| 14 | 30, 31 | 6.3 ^{+1.1} _{-1.5} | 67.2 ^{+13.7} _{-10.1} | 4.9 ^{+0.9} _{-0.7} | 2.0 ± 0.1 | 1.6 ^{+0.3} _{-0.2} | 23 ⁺¹⁶ ₋₅ | 285/337 | |
| 15 | 31, 32 | 7.1 ^{+1.3} _{-1.5} | 74.3 ^{+15.3} _{-10.6} | 4.5 ^{+0.8} _{-0.6} | 1.83 ± 0.07 | 1.5 ^{+0.2} _{-0.1} | 21 ⁺¹¹ ₋₄ | 397/337 | |
| 16 | 32, 34 | 8.3 ^{+0.8} _{-0.9} | 71 ⁺¹⁰ ₋₉ | 4.6 ^{+0.6} _{-0.5} | 1.9 ± 0.1 | 1.5 ^{+0.1} _{-0.1} | 19 ⁺⁴ ₋₂ | 437/337 | |
| 17 | 34, 35 | 7.6 ^{+1.3} _{-1.6} | 68 ⁺¹² ₋₁₁ | 4.8 ^{+1.0} _{-0.6} | 2 ± 0.1 | 1.5 ^{+0.2} _{-0.1} | 22 ⁺¹¹ ₋₄ | 291/337 | |
| 18 | 35, 36 | 7.0 ^{+1.2} _{-1.5} | 64 ⁺¹² ₋₁₁ | 5.0 ^{+1.0} _{-0.7} | 2 ± 0.1 | 1.6 ^{+0.2} _{-0.2} | 24 ⁺¹⁴ ₋₅ | 304/337 | |
| 19 | 36, 38 | 8.0 ^{+0.5} _{-0.6} | 30.0 ^{+6.4} _{-5.2} | 12.6 ^{+∞} _{-5.3} | 4.5 ± 0.5 | 1.6 ^{+0.1} _{-0.1} | 18 ⁺² ₋₈ | 395/337 | |
| 20 | 38, 39 | 7.5 ^{+0.5} _{-0.5} | 28.5 ^{+2.6} _{-2.5} | [10] | 4.7 ± 0.5 | 1.8 ^{+0.2} _{-0.2} | 18 ⁺² ₋₂ | 302/338 | |
| 21 | 39, 41 | 7.0 ^{+0.4} _{-0.5} | 50 ⁺²⁵ ₋₂₀ | 3.8 ^{+2.5} _{-0.9} | 2.7 ± 0.2 | 2.4 ^{+1.7} _{-0.6} | 20 ⁺³ ₋₂ | 388/337 | |
| 22 | 41, 44 | 7.0 ^{+0.4} _{-0.4} | 40 ⁺¹⁰ _{-8.4} | 5.8 ^{+2.7} _{-1.2} | 3.4 ± 0.3 | 2.0 ^{+0.3} _{-0.3} | 21 ⁺² ₋₂ | 448/337 | |
| 23 | 44, 45 | 6.0 ^{+0.9} _{-1.3} | 42 ⁺¹⁸ ₋₁₅ | 5.0 ^{+5.1} _{-1.3} | 3.2 ± 0.2 | 1.8 ^{+0.6} _{-0.3} | 25 ⁺¹⁴ ₋₃ | 177/337 | |
| 24 | 45, 46 | 7.8 ^{+0.8} _{-0.8} | 54 ⁺¹⁶ ₋₁₃ | 5.0 ^{+2.3} _{-1.1} | 2.5 ± 0.1 | 1.7 ^{+0.4} _{-0.2} | 19 ⁺⁴ ₋₃ | 310/337 | |
| 25 | 46, 47 | 7 ⁺¹ ₋₁ | 47 ⁺³² ₋₂₃ | 4.4 ^{+11.6} _{-1.4} | 2.9 ± 0.2 | 1.9 ^{+1.1} _{-0.4} | 20 ⁺⁷ ₋₃ | 314/337 | |
| 26 | 47, 48 | 7 ⁺¹ ₋₁ | 47 ⁺²⁵ ₋₁₈ | 5.0 ^{+6.2} _{-1.4} | 2.9 ± 0.2 | 2.8 ^{+∞} _{-0.9} | 19 ⁺⁶ ₋₃ | 290/337 | |
| 27 | 48, 50 | 6.1 ^{+0.7} _{-0.8} | 33 ⁺²⁴ ₋₁₇ | 5 ^{+∞} ₋₂ | 4.1 ± 0.4 | 2.2 ^{+2.1} _{-0.6} | 20 ⁺⁶ ₋₃ | 302/337 | |
| 28 | 50, 51 | 7 ⁺¹ ₋₁ | 27 ⁺²⁴ ₋₈ | 11 ^{+∞} ₋₇ | 5.1 ± 0.6 | 2.0 ^{+1.3} _{-0.4} | 16 ⁺⁶ ₋₂ | 267/337 | |
| 29 | 51, 53 | 6.8 ^{+0.6} _{-0.7} | 43 ⁺¹⁶ ₋₁₃ | 4.8 ⁺³ _{-1.1} | 3.1 ± 0.2 | 2.2 ^{+0.8} _{-0.4} | 20 ⁺⁵ ₋₃ | 335/337 | |
| 30 | 53, 55 | 6.4 ^{+0.6} _{-0.7} | 64 ⁺¹⁴ ₋₁₂ | 4.3 ^{+0.9} _{-0.6} | 2.1 ± 0.1 | 1.9 ^{+0.4} _{-0.3} | 23 ⁺⁵ ₋₃ | 387/337 | |
| 31 | 55, 56 | 7.2 ^{+1.1} _{-1.5} | 85 ⁺²⁰ ₋₁₈ | 3.9 ^{+0.8} _{-0.5} | 1.60 ± 0.06 | 2.3 ^{+1.2} _{-0.5} | 19 ⁺⁸ ₋₃ | 301/337 | |
| 32 | 56, 57 | 6.7 ^{+1.1} _{-1.3} | 83 ⁺²⁰ ₋₁₇ | 3.8 ^{+0.7} _{-0.5} | 1.60 ± 0.06 | 2.0 ^{+0.6} _{-0.3} | 24 ⁺¹¹ ₋₄ | 317/337 | |
| 33 | 57, 58 | 6.9 ^{+1.0} _{-1.3} | 78 ⁺¹⁶ ₋₁₄ | 4.0 ^{+0.7} _{-0.5} | 1.75 ± 0.07 | 2.1 ^{+0.6} _{-0.4} | 25 ⁺¹¹ ₋₄ | 349/337 | |
| 34 | 58, 59 | 7.0 ^{+1.0} _{-1.1} | 72 ⁺¹⁵ ₋₁₃ | 4.2 ^{+0.8} _{-0.6} | 1.9 ± 0.1 | 1.8 ^{+0.3} _{-0.2} | 24 ⁺⁹ ₋₄ | 359/337 | |
| 35 | 59, 60 | 6.9 ^{+1.0} _{-1.2} | 86 ⁺²⁰ ₋₁₈ | 3.5 ^{+0.6} _{-0.5} | 1.60 ± 0.06 | 2.0 ^{+0.5} _{-0.3} | 23 ⁺¹⁰ ₋₄ | 345/337 | |
| 36 | 60, 61 | 7.5 ^{+1.0} _{-1.2} | 81 ⁺²⁵ ₋₂₁ | 3.5 ^{+1.0} _{-0.6} | 1.67 ± 0.06 | 1.8 ^{+0.5} _{-0.3} | 21 ⁺⁷ ₋₃ | 315/337 | |
| 37 | 61, 63 | 6.7 ^{+0.7} _{-0.7} | 44 ⁺¹² ₋₁₀ | 5.6 ^{+2.5} _{-1.1} | 3.1 ± 0.2 | 1.5 ^{+0.2} _{-0.2} | 21 ⁺⁵ ₋₃ | 378/337 | |
| 38 | 63, 64 | 6.6 ^{+1.1} _{-1.4} | 45 ⁺²⁰ ₋₁₆ | 5 ⁺¹ ₋₁ | 3.0 ± 0.2 | 1.7 ^{+0.6} _{-0.3} | 19 ⁺¹¹ ₋₄ | 288/337 | |
| 39 | 64, 65 | 7.3 ^{+1.2} _{-1.8} | 82.7 ⁺³⁰ _{-25.2} | 3.3 ⁺¹ _{-0.6} | 1.60 ± 0.06 | 2.5 ^{+2.5} _{-0.7} | 19 ⁺⁷ ₋₄ | 277/337 | |
| 40 | 65, 67 | 7.5 ^{+0.5} _{-0.6} | 47 ⁺¹⁰ ₋₉ | 5.5 ^{+1.8} _{-1.0} | 2.9 ± 0.2 | 1.7 ^{+0.2} _{-0.2} | 21 ⁺³ ₋₂ | 447/337 | |
| 41 | 67, 68 | 7.1 ^{+0.7} _{-0.8} | 49 ⁺¹⁶ ₋₁₃ | 5 ^{+2.4} _{-1.1} | 2.8 ± 0.2 | 2.0 ^{+0.6} _{-0.3} | 23 ⁺⁶ ₋₃ | 366/337 | |
| 42 | 68, 69 | 7.0 ^{+0.7} _{-0.8} | 57 ⁺¹⁶ ₋₁₄ | 4.3 ^{+1.3} _{-0.7} | 2.4 ± 0.1 | 2.0 ^{+0.6} _{-0.3} | 26 ⁺⁶ ₋₃ | 323/337 | |
| 43 | 69, 70 | 6.6 ^{+1.1} _{-1.1} | 75 ⁺⁴² ₋₄₇ | 2.9 ^{+4.3} _{-0.7} | 1.8 ± 0.1 | 2.0 ^{+1.3} _{-0.6} | 24 ⁺⁸ ₋₃ | 335/337 | |
| 44 | 70, 71 | 7.4 ^{+0.7} _{-0.8} | 56 ⁺²¹ ₋₁₆ | 4.2 ^{+2.0} _{-0.9} | 2.4 ± 0.1 | 2.0 ^{+0.7} _{-0.3} | 21 ⁺⁴ ₋₃ | 308/337 | |
| 45 | 71, 72 | 7.2 ^{+0.7} _{-0.7} | 56 ⁺¹⁰ _{-9.5} | 4.8 ⁺¹ _{-0.7} | 2.4 ± 0.1 | 2.4 ^{+0.7} _{-0.4} | 24 ⁺⁵ ₋₃ | 306/337 | |
| 46 | 72, 73 | 7.4 ^{+0.7} _{-0.9} | 26 ⁺¹⁸ _{-6.2} | 11.8 ⁺⁵ ₋₇ | 5.2 ± 0.6 | 1.9 ^{+0.5} _{-0.2} | 20 ⁺⁵ ₋₂ | 274/337 | |
| 47 | 73, 74 | 7.0 ^{+0.5} _{-0.6} | 23.0 ^{+3.3} _{-3.2} | [10] | 6.0 ± 0.8 | 1.7 ^{+0.3} _{-0.2} | 20 ⁺³ ₋₂ | 275/338 | |
| 48 | 74, 76 | 7.2 ^{+0.5} _{-0.5} | 25.0 ^{+11.7} _{-6.4} | 12.8 ^{+∞} _{-7.2} | 5.5 ± 0.6 | 1.8 ^{+0.2} _{-0.2} | -20 ⁺³ ₋₂ | 406/337 | |
| 49 | 76, 77 | 6.7 ^{+0.9} _{-1.3} | 45 ⁺²⁸ ₋₂₁ | 4.3 ^{+6.4} _{-1.25} | 3.0 ± 0.2 | 2.4 ^{+3.7} _{-0.7} | 19 ⁺¹⁰ ₋₃ | 284/337 | |
| 50 | 77, 78 | 7.2 ^{+0.9} ₋₁ | 52 ⁺³⁴ ₋₂₇ | 4.0 ^{+8.4} _{-1.2} | 2.6 ± 0.2 | 2.3 ⁺⁴ _{-0.7} | 18 ⁺⁵ ₋₃ | 270/337 | |
| 51 | 78, 82 | [7] | 24 ^{+8.2} _{-5.5} | 11 ^{+∞} ₋₅ | 5.7 ± 0.7 | 2 ^{+0.2} _{-0.2} | 15.3 ^{+0.2} _{-0.2} | 384/338 | |
| 52 | 82, 84 | 7.4 ^{+0.7} _{-0.7} | 38.4 ^{+17.1} _{-12.3} | 6 ^{+8.6} _{-1.9} | 3.5 ± 0.3 | 1.4 ^{+0.3} _{-0.2} | 16 ⁺³ ₋₂ | 375/337 | |
| 53 | 84, 85 | 7 ⁺¹ ₋₁ | 38 ⁺⁶ ₋₆ | [6] | 3.6 ± 0.3 | 2.0 ^{+0.8} _{-0.5} | 14 ⁺² ₋₂ | 237/338 | |
| 54 | 85, 90 | 6.6 ^{+0.5} _{-0.5} | 32 ⁺¹⁹ ₋₁₅ | 5.8 ^{+∞} ₋₂ | 4.2 ± 0.4 | 2.0 ^{+0.6} _{-0.3} | 15 ⁺² ₋₂ | 462/337 | |
| 55 | 90, 101 | 6.1 ^{+0.4} _{-0.4} | 30 ^{+3.4} _{-3.4} | [6] | 4.5 ± 0.4 | 1.7 ^{+0.3} _{-0.2} | 12 ⁺² ₋₁ | 473/338 | |
| 56 | 101, 113 | 6.5 ^{+0.6} _{-0.6} | 39 ⁺²⁰ ₋₁₅ | 5.0 ^{+8.3} _{-1.6} | 3.5 ± 0.3 | 2.2 ^{+1.5} _{-0.5} | 9 ⁺² ₋₁ | 437/337 | |
| 57 | 113, 136 | 5.8 ^{+0.5} _{-0.5} | 25 ⁺¹⁷ ₋₁₀ | 7.8 ^{+∞} _{-3.4} | 2.0 ± 0.1 | 1.9 ^{+1.0} _{-0.4} | 11 ⁺² ₋₁ | 603/337 | |
| 58 | 136, 137 | 5.8 ^{+1.1} ₋₂ | 67 ⁺²⁶ ₋₂₆ | 3.5 ^{+1.9} _{-0.8} | 2.0 ± 0.1 | 30 ^{+∞} ₋₂₇ | 17 ⁺¹⁸ ₋₄ | 256/337 | |
| 59 | 137, 150 | 5.6 ^{+0.6} _{-0.7} | 28 ⁺¹⁶ ₋₁₂ | 6.6 ⁺¹⁶⁰ _{-2.3} | 4.8 ± 0.5 | 2.2 ^{+1.4} _{-0.5} | 12 ⁺⁴ ₋₂ | 462/337 | |
| 60 | 150, 171 | 4.5 ^{+0.9} _{-1.7} | 61 ⁺¹⁴⁶ ₋₅₀ | 3.0 ^{+2.1} _{-1.3} | 2.2 ± 0.1 | 3.4 ^{+∞} _{-2.0} | 13 ⁺¹⁹ ₋₃ | 372/337 | |

Table 5. Time-resolved Spectral fitting (continued)

| Synchrotron model | | | | | |
|-------------------|-----------------------------------|---------------------|--------------------------|------------------------|------------|
| Sr. no. | (t ₁ ,t ₂) | $\gamma m/\gamma c$ | E_c (keV) | p | pgstat/dof |
| 1 | -1, 7 | $3.6^{+0.5}_{-1.4}$ | $18.2^{+3.4}_{-5.7}$ | > 3.04 | 420/339 |
| 2 | 7, 9 | $3.7^{+3.5}_{-2.1}$ | $29.6^{+22.0}_{-12.1}$ | > 2.33 | 286/339 |
| 3 | 9, 10 | $3.5^{+0.8}_{-2.1}$ | $41.2^{+15.0}_{-13.2}$ | > 2.43 | 214/339 |
| 4 | 10, 12 | $5.0^{+1.4}_{-1.6}$ | $45.2^{+8.7}_{-6.5}$ | > 2.98 | 296/339 |
| 5 | 12, 14 | $4.1^{+0.7}_{-1.3}$ | $69.8^{+12.4}_{-8.9}$ | > 3.18 | 302/339 |
| 6 | 14, 17 | $4.8^{+1.3}_{-0.8}$ | $60.5^{+11.3}_{-7.4}$ | > 2.69 | 384/339 |
| 7 | 17, 18 | $2.6^{+0.9}_{-2.1}$ | $62.4^{+125.8}_{-11.3}$ | > 2.86 | 285/339 |
| 8 | 18, 19 | $1.8^{+0.8}_{-0.8}$ | $81.9^{+150.7}_{-19.2}$ | $3.93^{+0.89}_{-0.87}$ | 207/339 |
| 9 | 19, 20 | $1.9^{+0.8}_{-0.9}$ | $84.8^{+146.3}_{-17.9}$ | > 3.41 | 334/339 |
| 10 | 20, 24 | $1.6^{+0.1}_{-0.3}$ | $89.5^{+133.7}_{-10.5}$ | $3.88^{+0.54}_{-0.37}$ | 602/339 |
| 11 | 24, 26 | $2.3^{+0.3}_{-0.7}$ | $35.4^{+7.3}_{-2.3}$ | > 3.28 | 434/339 |
| 12 | 26, 29 | $3.3^{+0.1}_{-0.3}$ | $32.8^{+0.9}_{-2.6}$ | > 4.24 | 558/339 |
| 13 | 29, 30 | $3.1^{+0.6}_{-0.7}$ | $51.7^{+10.7}_{-6.9}$ | > 3.81 | 311/339 |
| 14 | 30, 31 | $2.3^{+0.5}_{-0.4}$ | $77.6^{+11.9}_{-12.1}$ | > 4.13 | 298/339 |
| 15 | 31, 32 | $2.3^{+0.4}_{-0.5}$ | $90.9^{+20.5}_{-6.4}$ | > 4.09 | 406/339 |
| 16 | 32, 34 | $1.8^{+0.3}_{-0.1}$ | $99.4^{+19.2}_{-10.4}$ | > 3.62 | 485/339 |
| 17 | 34, 35 | $1.5^{+0.6}_{-0.2}$ | $113.7^{+200.9}_{-19.9}$ | > 3.37 | 304/339 |
| 18 | 35, 36 | $2.1^{+0.2}_{-0.8}$ | $81.4^{+85.8}_{-5.3}$ | > 4.33 | 314/339 |
| 19 | 36, 38 | $1.7^{+0.0}_{-0.7}$ | $62.9^{+1.2}_{-12.6}$ | $3.60^{+0.34}_{-0.27}$ | 478/339 |
| 20 | 38, 39 | $2.3^{+0.5}_{-0.7}$ | $26.1^{+6.0}_{-4.3}$ | > 3.56 | 347/339 |
| 21 | 39, 41 | $2.7^{+0.1}_{-0.6}$ | $15.5^{+2.5}_{-1.4}$ | > 3.67 | 470/339 |
| 22 | 41, 44 | $3.5^{+0.2}_{-0.3}$ | $14.9^{+1.8}_{-0.9}$ | > 4.55 | 572/339 |
| 23 | 44, 45 | $2.4^{+0.1}_{-0.6}$ | $30.2^{+6.5}_{-3.3}$ | > 3.77 | 285/339 |
| 24 | 45, 46 | $2.9^{+0.1}_{-0.4}$ | $37.6^{+2.4}_{-5.2}$ | > 3.89 | 364/339 |
| 25 | 46, 47 | $2.8^{+0.5}_{-0.8}$ | $22.9^{+4.9}_{-3.4}$ | > 3.41 | 339/339 |
| 26 | 47, 48 | $2.5^{+0.1}_{-0.5}$ | $19.7^{+1.4}_{-3.4}$ | > 3.99 | 321/339 |
| 27 | 48, 50 | $2.7^{+0.1}_{-0.8}$ | $13.2^{+3.2}_{-1.7}$ | > 3.45 | 326/339 |
| 28 | 50, 51 | $2.0^{+0.2}_{-0.6}$ | $26.3^{+6.0}_{-6.5}$ | > 3.58 | 287/339 |
| 29 | 51, 53 | $2.5^{+0.1}_{-0.5}$ | $23.0^{+3.9}_{-1.2}$ | > 3.99 | 378/339 |
| 30 | 53, 55 | $3.5^{+0.4}_{-0.5}$ | $30.1^{+4.0}_{-2.8}$ | > 4.28 | 446/339 |
| 31 | 55, 56 | $2.6^{+0.1}_{-0.4}$ | $53.3^{+6.2}_{-8.5}$ | > 4.04 | 345/339 |
| 32 | 56, 57 | $3.0^{+0.5}_{-0.5}$ | $47.3^{+7.3}_{-5.3}$ | > 4.20 | 351/339 |
| 33 | 57, 58 | $2.8^{+0.4}_{-0.5}$ | $50.8^{+7.8}_{-5.4}$ | > 4.10 | 392/339 |
| 34 | 58, 59 | $2.8^{+0.4}_{-0.4}$ | $50.7^{+6.4}_{-5.7}$ | > 4.05 | 397/339 |
| 35 | 59, 60 | $3.3^{+0.6}_{-0.4}$ | $40.5^{+4.8}_{-4.8}$ | > 4.13 | 374/339 |
| 36 | 60, 61 | $3.2^{+0.4}_{-0.5}$ | $40.7^{+4.9}_{-4.1}$ | > 4.05 | 346/339 |
| 37 | 61, 63 | $2.9^{+0.1}_{-0.6}$ | $36.0^{+4.2}_{-1.1}$ | > 3.66 | 414/339 |
| 38 | 63, 64 | $2.2^{+0.3}_{-1.5}$ | $39.5^{+69.8}_{-6.6}$ | > 3.02 | 302/339 |
| 39 | 64, 65 | $2.7^{+0.5}_{-0.6}$ | $34.0^{+6.4}_{-4.7}$ | > 3.90 | 300/339 |
| 40 | 65, 67 | $2.5^{+0.5}_{-0.3}$ | $40.0^{+1.8}_{-3.1}$ | > 4.39 | 531/339 |
| 41 | 67, 68 | $2.5^{+0.1}_{-0.4}$ | $31.4^{+4.0}_{-4.3}$ | > 3.98 | 406/339 |
| 42 | 68, 69 | $2.7^{+0.3}_{-0.4}$ | $33.3^{+4.5}_{-3.4}$ | > 4.01 | 367/339 |
| 43 | 69, 70 | $2.9^{+0.1}_{-0.8}$ | $19.5^{+4.1}_{-2.2}$ | > 3.42 | 361/339 |
| 44 | 70, 71 | $3.1^{+0.4}_{-0.5}$ | $25.4^{+4.0}_{-3.0}$ | > 3.92 | 358/339 |
| 45 | 71, 72 | $2.0^{+0.1}_{-0.3}$ | $44.7^{+6.3}_{-5.6}$ | > 4.54 | 372/339 |
| 46 | 72, 73 | $2.2^{+0.4}_{-0.6}$ | $25.0^{+5.3}_{-3.7}$ | > 3.77 | 305/339 |
| 47 | 73, 74 | $2.5^{+0.7}_{-0.9}$ | $14.9^{+5.8}_{-3.3}$ | > 2.97 | 303/339 |
| 48 | 74, 76 | $2.5^{+0.1}_{-0.4}$ | $20.5^{+2.9}_{-1.6}$ | > 3.96 | 481/339 |
| 49 | 76, 77 | $2.3^{+0.5}_{-0.8}$ | $21.4^{+6.2}_{-4.1}$ | > 3.40 | 303/339 |
| 50 | 77, 78 | $2.8^{+0.1}_{-0.8}$ | $17.7^{+4.2}_{-2.3}$ | > 3.36 | 300/339 |
| 51 | 78, 82 | $2.9^{+0.6}_{-0.7}$ | $13.6^{+2.3}_{-1.7}$ | > 3.31 | 465/339 |
| 52 | 82, 84 | $3.2^{+1.0}_{-1.0}$ | $24.0^{+4.4}_{-3.4}$ | > 2.68 | 427/339 |
| 53 | 84, 85 | $3.1^{+0.4}_{-1.3}$ | $19.2^{+8.2}_{-3.8}$ | > 2.98 | 250/339 |
| 54 | 85, 90 | $2.8^{+0.1}_{-0.6}$ | $15.0^{+2.5}_{-1.3}$ | > 3.60 | 524/339 |
| 55 | 90, 101 | $3.2^{+0.2}_{-1.1}$ | $14.2^{+3.2}_{-1.3}$ | > 2.95 | 511/339 |
| 56 | 101, 113 | $3.3^{+0.2}_{-0.7}$ | $12.8^{+2.3}_{-1.2}$ | > 3.52 | 485/339 |
| 57 | 113, 136 | $2.9^{+0.1}_{-0.6}$ | $11.3^{+1.9}_{-1.7}$ | > 3.72 | 654/339 |
| 58 | 136, 137 | $3.0^{+1.2}_{-1.0}$ | $13.0^{+1.8}_{-4.6}$ | > 3.39 | 265/339 |
| 59 | 137, 150 | $3.0^{+0.8}_{-0.6}$ | $11.2^{+2.4}_{-1.2}$ | > 3.70 | 485/339 |
| 60 | 150, 171 | $2.1^{+1.6}_{-1.7}$ | $7.6^{+15.5}_{-3.3}$ | > 2.56 | 378/339 |

- Sari, R., Piran, T., & Narayan, R. 1998, *ApJL*, 497, L17
- Scargle, J. D., Norris, J. P., Jackson, B., & Chiang, J. 2013, *ApJ*, 764, 167
- Tavani, M. 1996, *ApJ*, 466, 768
- Tierney, D., McBreen, S., Preece, R. D., et al. 2013, *A&A*, 550, A102
- Titarchuk, L., Farinelli, R., Frontera, F., & Amati, L. 2012, *ApJ*, 752, 116
- Vadawale, S. V., Chattopadhyay, T., Rao, A. R., et al. 2015, *Astronomy & Astrophysics*, 578, 73
- Vadawale, S. V., Chattopadhyay, T., Mithun, N. P. S., et al. 2017, *Nature Astronomy*, doi:10.1038/s41550-017-0293-z
- Vianello, G., Gill, R., Granot, J., et al. 2017, *ArXiv e-prints*, arXiv:1706.01481
- Vurm, I., & Beloborodov, A. M. 2016, *ApJ*, 831, 175
- Wang, X.-G., Zhang, B., Liang, E.-W., et al. 2018, *ApJ*, 859, 160
- Wang, Y.-Z., Wang, H., Zhang, S., et al. 2017, *ApJ*, 836, 81
- Willingale, R., Starling, R. L. C., Beardmore, A. P., Tanvir, N. R., & O'Brien, P. T. 2013, *MNRAS*, 431, 394
- Woosley, S. E., & Bloom, J. S. 2006, *ARA&A*, 44, 507
- Zhang, B., Fan, Y. Z., Dyks, J., et al. 2006, *ApJ*, 642, 354
- Zhang, B., & Yan, H. 2011, *ApJ*, 726, 90
- Zhang, B.-B., Uhm, Z. L., Connaughton, V., Briggs, M. S., & Zhang, B. 2016, *ApJ*, 816, 72
- Zhang, B.-B., Zhang, B., Castro-Tirado, A. J., et al. 2018, *Nature Astronomy*, 2, 69
- Zheng, W., Shen, R. F., Sakamoto, T., et al. 2012, *ApJ*, 751, 90